Upstream flow effects revealed in the EastGRIP ice core using a Monte Carlo inversion of a two-dimensional ice-flow model

Tamara Annina Gerber[1], Christine Schøtt Hvidberg[1], Sune Olander Rasmussen[1], Steven Franke[2], Giulia Sinnl[1], Aslak Grinsted[1], Daniela Jansen[2], and Dorthe Dahl-Jensen[1, 3]

[1]Section for the Physics of Ice, Climate and Earth, The Niels Bohr Institute, University of Copenhagen, Copenhagen, Denmark
[2]Alfred Wegener Institute, Helmholtz Centre for Polar and Marine Research, Bremerhaven, Germany
[3]Centre for Earth Observation Science, University of Manitoba, Winnipeg, Canada

Correspondence: Tamara Annina Gerber (tamara.gerber@nbi.ku.dk)

Abstract. The Northeast Greenland Ice Stream (NEGIS) is the largest active ice stream on the Greenland Ice Sheet (GrIS) and a crucial contributor to the ice-sheet mass balance. To investigate the ice-stream dynamics and to gain information about the past climate, a deep ice core is drilled in the upstream part of the NEGIS, termed the East Greenland Ice-Core Project (EastGRIP). Upstream flow effects introduce ~~non-climatic~~ climatic bias in ice cores through the advection of ice deposited under different conditions further upstream, and are particularly strong at EastGRIP due to ~~high ice-flow velocities and the~~ its location inside an ice stream on the eastern flank of the GrIS. Understanding and ultimately correcting for such effects requires information on the ~~source area and the local~~ atmospheric conditions at the time ~~of ice~~ and location of snow deposition. We use a two-dimensional Dansgaard–Johnsen model to simulate ice flow along three approximated flow lines between the summit of the ice sheet (GRIP) and EastGRIP. ~~Model parameters are determined using a Monte Carlo inversion by minimizing the misfit between modelled isochrones and isochrones observed~~ Isochrones are traced in radio-echo-sounding ~~(RES) images~~ images along these flow lines and dated with the GRIP and EastGRIP ice core chronologies. The observed depth-age relationship constrains the Monte Carlo method which is used to determine unknown model parameters. We calculate backward-in-time particle trajectories to determine the source ~~area~~ location of ice found in the EastGRIP ice core and present estimates of surface elevation and past accumulation rates at the deposition site. Our results indicate that increased ~~accumulation in the upstream area~~ snow accumulation with increasing upstream distance is predominantly responsible for the constant annual layer thicknesses observed in the upper part of the ice column at EastGRIP ~~. Inverted~~ and the inverted model parameters suggest that ~~the imprint of~~ basal melting and sliding ~~is present in large segments along the flow profiles and that most internal ice deformation happens in the lower half of the ice column~~are important factors determining ice flow in the NEGIS. The results of this study ~~act as~~ form a basis for applying upstream corrections to a variety of ice-core measurements, and the inverted model parameters are useful constraints for more sophisticated modelling approaches in the future.

Copyright statement.

1 Introduction

The East Greenland Ice-Core Project (EastGRIP) is the first attempt to retrieve a deep ice core inside an active ice stream. The drill site is located in the upstream part of the Northeast Greenland Ice Stream (NEGIS, Fahnestock et al., 1993), which is a substantial contributor to the Greenland Ice Sheet (GrIS) mass balance (Khan et al., 2014) and accounts for around 12 % of its total ice discharge (Rignot and Mouginot, 2012). ~~Understanding the driving mechanisms of the NEGIS is essential to anticipate its future development and~~ Large-scale ice-sheet models are essential tools to anticipate the future development of the NEGIS and its potential impact on the ~~ice-sheet stability with large-scale ice-flow models (Joughin et al., 2001; Khan et al., 2014; Vallelonga et al., 201~~ ~~. Yet, many unknowns remain in our comprehension of ice-stream dynamics (Tulaczyk et al., 2000; Robel et al., 2013), and the underlying processes~~ stability of the GrIS (Joughin et al., 2001; Khan et al., 2014; Vallelonga et al., 2014). However, results obtained from such models often show a significant deviation from observed surface velocitites in the NEGIS and its catchment area (Aschwanden et al., 2016; Mottram et al., 2019). In particular, the high ice flow velocities in the upstream area of the NEGIS and the clearly defined shear margins are difficult to be reproduced by ice flow models (Beyer et al., 2018). A recent study by Smith-Johnsen et al. (2020a) showed, that the high surface velocities in the onset region of the ice stream could be reproduced with their model, using an exceptionally high and geologically unfeasible geothermal heat flux (Bons et al., 2021) . This indicates that additional, yet unknown processes must facilitate ice flow in the NEGIS and that the driving mechanisms governing ice flow are ~~not sufficiently understoodto successfully reproduce the NEGIS in sophisticated ice-sheet models (e.g. Mottram et al., 2019; Shepherd et al., 2020)~~still not well enough understood. The EastGRIP ice core sheds some light on the key processes ~~, as it reveals~~ by revealing unique information about ice dynamics, stress regimes, temperatures and basal properties, all of which are crucial components in ice-flow models.

Chemical and physical ~~parameters~~ properties measured in ice cores reflect the atmospheric conditions at the time and location of snow deposition (e.g. Alley et al., 1993; Petit et al., 1999; Andersen et al., 2004; Marcott et al., 2014). Most of the deep drilling projects in Greenland and Antarctica are located in slow-moving areas at ice domes or near ice divides (e.g. GRIP ~~(Dahl-Jensen et al., 1993)~~(Dansgaard et al., 1982), Dome Fuji (Ageta et al., 1998), Dome C (Parrenin et al., 2007)), ~~where~~ so the ice core represents climate records from this fixed location. For ice cores drilled on the flank of an ice sheet (e.g. GISP2 (Meese et al., 1997), Vostok (Lorius et al., 1985; Petit et al., 1999)) or in areas with higher flow velocities (e.g. Camp Century (Dansgaard and Johnsen, 1969), Byrd (Gow et al., 1968), NorthGRIP (Andersen et al., 2004), EDML (Barbante et al., 2006), WAIS Divide (Fudge et al., 2013), NEEM (NEEM Community members et al., 2013)), the ice found at depth was originally deposited further upstream and advected with the ~~lateral flow~~horizontal flow.

The spatial variation in accumulation rate, surface temperature and atmospheric pressure ~~in the upstream area can introduce non-climatic~~ can introduce climatic imprints in the ice core ~~(e.g. Koutnik et al., 2016; Fudge et al., 2020)~~record which stem from the advection of ice deposited under different conditions further upstream. The ice core signal is thus a combination of temporal and spatial variations in climatic components (Fudge et al., 2020). The magnitude of these so-called upstream effects depends on the ice-flow velocity, ~~spatially variable~~ spatial variability of the precipitation and the sensitivity to atmospheric variations of the ~~parameter~~ quantity under consideration. While well-mixed atmospheric gases, such as carbon dioxide or methane,

and dry-deposited impurities are barely affected (Fudge et al., 2020), properties extracted from the ice phase can show significant bias~~which needs to be taken into account to ensure accurate data interpretation~~. Affected measurements include aerosols and cosmogenic isotopes, such as ^{10}Be (Yiou et al., 1997; Finkel and Nishiizumi, 1997; Raisbeck et al., 2007; Delaygue and Bard, 2011), the isotopic composition of water (Dansgaard, 1964; Jouzel et al., 1997; Aizen et al., 2006), the total air content (Raynaud et al., 1997; Eicher et al., 2016) and ice temperatures (Salamatin et al., 1998). Processes such as vertical thinning of the ice column and firn densification are also influenced by upstream effects and have consequences on the annual layer thicknesses (Dahl-Jensen et al., 1993; Rasmussen et al., 2006; Svensson et al., 2008) and the age difference between ice and the enclosed air (Herron and Langway, 1980; Alley et al., 1982). Upstream effects in the EastGRIP ice core are expected to be particularly strong due to the fast ice flow in the upstream area (57 ma^{-1} at EastGRIP, Hvidberg et al., 2020), the strong gradient in the accumulation rate across Greenland's main ice ridge (Burgess et al., 2010), and the increasing elevation towards the central ice divide (Simonsen and Sørensen, 2017). The correction of these effects in the EastGRIP ice core is necessary to interpret the ice core measurements within the climatic context and requires information on the conditions at the time and location of snow deposition.

Post-depositional deformation of isochrones observed in radio-echo-sounding (RES) images along flow lines provides information on ice-flow dynamics and can be used to reconstruct past and present flow characteristics. In this study, we use a vertically two-dimensional Dansgaard–Johnsen model to simulate the ~~ice flow~~ propagation and deformation of isochrones along three approximated flow lines between the ice-sheet summit (GRIP) and EastGRIP. ~~Model parameters are sampled during a Monte Carlo inversion~~ A Monte Carlo method is used to determine the unknown model parameters by minimizing the misfit between modelled ~~isochrones and~~ and observed data. The latter includes the depth of isochrones observed in ~~radio-echo-sounding (RES) images of known depth and age. From the resulting flow model~~RES images along the flow lines and a parameter α_{sur} representing the sum of the horizontal strain rates deduced from satellite based surface velocities. From the modelled velocity field, we calculate particle trajectories backwards in time to ~~determine the source area~~ infer the source location of ice found in the EastGRIP ice core and estimate the accumulation rate at the time of snow deposition. The ~~results presented here serve as a basis for corrections of~~ source characteristics presented here form a basis to correct for upstream effects in various chemical and physical quantities of the EastGRIP ice core. These corrections are important to remove any climatic bias in ice-core measurements which are currently analyzed and will become available in the future. The inverted model parameters give insight into basal properties and ice-flow dynamics along the flow lines and can be used to constrain more sophisticated numerical models of the NEGIS.

2 Data and methods

Snow layers deposited at the surface of ice sheets are buried with time and are deformed as a consequence of ice flow. While these isochrones can be observed in RES images today, the ice flow characteristics which shaped them are generally unknown. This is a typical geophysical inverse problem and can be formulated as $\mathbf{d} = g(\mathbf{m})$, where the function $g(\mathbf{m})$ represents the ice flow model linking the model parameters ($\mathbf{m}$) with the observed data ($\mathbf{d}$). A variety of inverse methods exist to find the model

parameters which reproduce the observed data within their uncertainties. Here, we use a Markov Chain Monte Carlo method to determine the unknown parameters of a two-dimensional ice flow model by minimizing the misfit between modelled and observed isochrones and strain rates. This allows us to reconstruct the ice flow characteristics in the past and to determine the flow trajectories of the EastGRIP ice.

In the coming sections we describe the data and methods underlying our results according to the work flow illustrated in Fig. 2. In Sect. 2.1 to 2.4 we explain how the isochrone depth-age relationship constraining the Monte Carlo method was obtained. This involves the selection of RES images approximating the EastGRIP flow line (Sect. 2.1), extending the existing chronology of the EastGRIP ice core to the current drill depth (Sect. 2.2), and the tracing and dating of isochrones in the RES data (Sect. 2.3). In Sect. 2.4 the ice flow model is described in detail and in Sect. 2.5 we elaborate on the Monte Carlo method used for parameter sampling. The section numbers are displayed in the corresponding steps in Fig. 2.

2.1 EastGRIP flow lines

~~The upstream flow path of ice found in the EastGRIP ice core can be estimated from present-day surface velocities. Many~~ Determining the exact flow line through the EastGRIP ice core site is important to understand the flow history of the survey area and enables us to reconstruct the location where the ice from the ice core was deposited at the ice sheet surface. For this, we use high-resolution satellite-based ~~velocity products are available. However, as a consequence of error propagation, minor uncertainties and bias in the data severely affect the tracking of flow lines along the velocity field (Hvidberg et al., 2020). We derived flow lines from different~~ surface velocity products ~~(e.g. Joughin et al., 2018; Gardner et al., 2020; Andersen et al., 2020, see Supple , and the diversity of these lines illustrates the uncertainties affecting~~ (e.g. Joughin et al., 2018; Gardner et al., 2020; Andersen et al., 2020, s to calculate the upstream flow path. Minor uncertainties and bias in these data products affect along-flow ~~tracking. The flow-line deviations between different products become considerably larger~~ tracing and lead to deviations between flow lines derived from different velocity maps. These deviations become more pronounced with increasing distance from ~~EastGRIP as a result of error propagation and larger uncertainties attributed to~~ the starting point, as the uncertainties propagate along the line and in general become larger in slow-moving areas ~~.~~ of the ice sheet (Hvidberg et al., 2020). Due to the small bias, we consider the DTU_SPACE (Andersen et al., 2020) line the most likely current flow line (Fig. 1b). Yet, there is no evidence that the present-day velocity field was the same in the past. A slight shift in the NEGIS shear margins or the central ice divide, for instance, would have a large effect on the velocity field and, hence, the determination of the flow line ~~through EastGRIP~~ of the EastGRIP ice remains ambiguous.

RES data reveal the internal structure of glaciers and ice sheets and provide valuable information on the ice flow characteristics, particularly when recorded parallel to the ice flow. The electromagnetic waves used in RES are sensitive to contrasts in dielectric properties of the medium they propagate. In ice sheets, these contrasts arise through density variations in the uppermost part of the ice column (Robin et al., 1969), changes in the crystal orientation fabric (Harrison, 1973), and impurity layers such as volcanic deposits (Paren and Robin, 1975). The latter is the most common reflector type below the firn (Millar, 1982; Eisen et al., 2006) , and because it is related to layers deposited over a relatively short period of time, most internal reflection horizons (IRHs) detected by RES can be considered isochrones.

~~(a) Overview of past and ongoing deep ice-core drilling projects on the GrIS (surface elevation and Greenland contour lines by Simonsen and Sørensen, 2017; Greene et al., 2017) and the outline of the study area. The NEGIS appears as a distinct feature in the surface velocities (Joughin et al., 2018). It extends from the central ice divide to the northeastern coast, where it splits up into the three marine-terminating glaciers 79N Glacier, Zachariae Isbræ and Storstrømmen Glacier. (b) The present-day EastGRIP flow line is derived from the DTU_SPACE surface velocity product (Andersen et al., 2020). Due to the limited availability of radar data along the flow line, we construct three approximate flow lines through a combination of various radar products (profile A–C) between GRIP and EastGRIP. Flow line B and C lack data in the centre of the profiles, marked as a dashed line. The downstream parts of line A and B comprise the same radar profile, which crosses the southern shear margin 82 km upstream of EastGRIP.~~

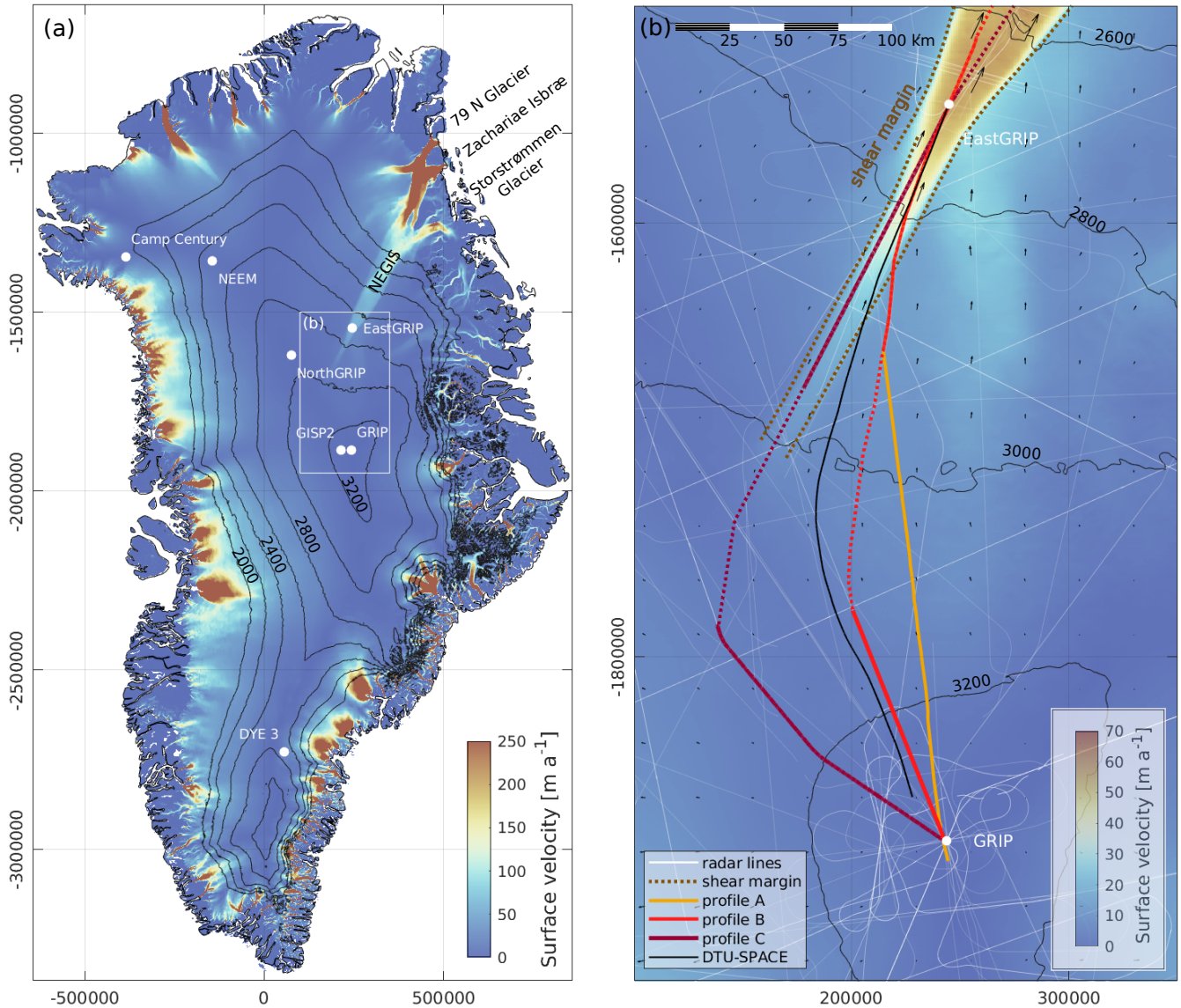

Figure 1. (a) Overview of past and ongoing deep ice-core drilling projects on the GrIS (surface elevation and Greenland contour lines by Simonsen and Sørensen, 2017; Greene et al., 2017) and the outline of the study area. The NEGIS appears as a distinct feature in the surface velocities (Joughin et al., 2018). It extends from the central ice divide to the northeastern coast, where it splits up into the three marine-terminating glaciers 79N Glacier, Zachariae Isbræ and Storstrømmen Glacier. (b) The present-day EastGRIP flow line is derived from the DTU_SPACE surface velocity product (Andersen et al., 2020). Due to the

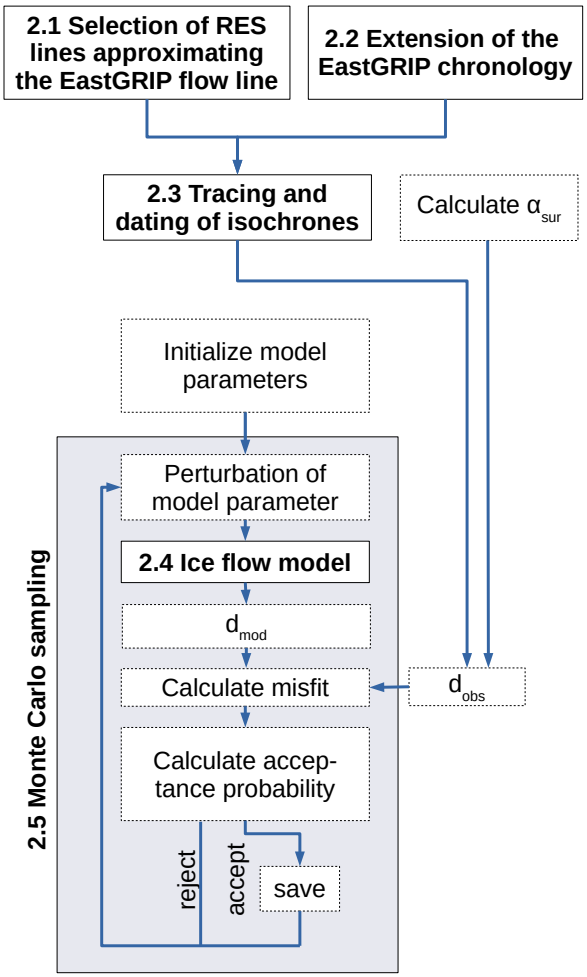

Figure 2. Workflow of the applied steps leading to the results described in Sect 3. The main steps are described in Sect. 2.1 to 2.5 and marked with the corresponding numbers in the figure: The observed data ($\mathbf{d}_{obs}$) constraining the Monte Carlo method consists of the α_{sur} calculated from the ice surface velocities and the isochrone depths along the flow lines. The latter is obtained by approximating the EastGRIP flow line with selected RES images (Sect. 2.1), extending the EastGRIP chronology to the current drill depth (Sect. 2.2) and subsequent tracing and dating of isochrones (Sect. 2.3). The iterative Monte Carlo sampling process is illustrated in the grey box (Sect. 2.5) and includes data simulation by a Dansgaard-Johnsen ice flow model described in Sect. 2.4.

The availability of RES data in the study area is limited, and unfortunately, the flight lines generally do not follow the surface velocity field. We have thus composed three approximated flow lines connecting the EastGRIP (75.63° N, 35.99° W, 2720 m) and the GRIP (72.58° N, 37.63° W, 3230 m) drill sites from the available RES data sets (Fig. 1b). The radar data used in this study (Table 1) were measured by the Alfred Wegener Institute, Helmholtz Centre for Polar and Marine Research (AWI, Jansen et al., 2020; Franke et al., 2021b) and the Centre for Remote Sensing of Ice Sheets (CReSIS, 2020). The AWI data were recorded by an 8-antenna-element ultra-wideband radar system (MCoRDS5) mounted on the Polar 6 Basler BT-67 aircraft, operating at a frequency range of 180–210 MHz (Franke et al., 2020, 2021b). The CReSIS radar data were measured by a ICORDS 2 (1999) and a MCoRDS 2 (2012) radar system, mounted on a P3 aircraft, at a frequency range of 141.5–158.5 MHz and 180–210 MHz, respectively. Details of the three radar systems are provided in Table 2.

The downstream parts of profile A and B consist of the same flight line, which passes through the EastGRIP ~~camp and crosses~~ drill site and intersects the southern shear margin around 82 km upstream of EastGRIP. Outside the NEGIS, the two lines split up and connect to two different RES profiles. Line B remains relatively close to the flow direction of the DTU_SPACE line but has a wide data gap in the centre of the profile. In line A, this problem is circumvented by using a radar profile connecting directly to GRIP, which ~~has the consequence of a deviation~~ deviates from the observed surface flow field ~~of~~ by more than 15 degrees ~~in some parts~~at some locations. Profile C follows the NEGIS trunk all the way to the central ice divide and connects to GRIP over the ice ridge without crossing the shear margin. Similar to flow line B, flow line C contains a substantial data gap between the onset region of the NEGIS and the central ice divide.

To avoid uncertainties related to the proximity of the model boundaries, the flow lines were extended more than 50 km beyond EastGRIP and have a total length of ~~423~~ 422 (line A), ~~422~~ 421 (line B) and 480 km (line C). ~~The radar data used in this study (Table 1) were measured by the Alfred Wegener Institute (AWI, Jansen et al., 2020; Franke et al., 2021b, in prep.) and the centre for Remote Sensing of Ice Sheets (CReSIS, 2020). The AWI data were recorded by an 8-antenna-element ultra-wideband radar system (MCoRDS5) mounted on the Polar 6 Basler BT-67 aircraft, operating at a frequency range of 180–210 (Franke et al., 2020, 2021b, in prep.). The CReSIS radar data were measured by a ICORDS 2 (1999) and MCoRDS 2 (2012) radar system, mounted on a P3 aeroplane, with a frequency range of 141.5–158.5 and 180–210 , respectively. Details of the three radar systems are provided in Table 2.~~ To account for any differences in surface elevation or topography between RES data from different years, the ice surface ~~reflection~~ reflections of the radar profiles ~~was~~ were aligned to the surface elevation from the Arctic DEM (digital elevation model, Porter et al., 2018). The bed topography in the data gaps of the profiles was derived from the BedMachine v3 data set (Morlighem et al., 2017).

2.2 ~~Stratigraphy~~

2.1.1 ~~Extending the chronology of EastGRIP from GS-2 to GS-14~~

~~Mojtabavi et al. (2020) synchronized the EastGRIP and NorthGRIP ice cores for the last 15 kyr in order to apply the~~

2.2 Extending the chronology of EastGRIP from GS-2 to GI-14

Table 1. ~~Radio-echo-sounding~~ RES profiles used to approximate the EastGRIP flow lines A–C. The data sets were measured between 1999 and 2018 by ~~the centre for Remote Sensing of Ice Sheets (~~CReSIS ~~, University of Kansas,)~~ (CReSIS, 2020) and ~~the Alfred Wegener Institute (AWI, Jansen et al., 2020; Franke et al., 2021b, in prep.)~~AWI (Jansen et al., 2020; Franke et al., 2021b).

Flow line	Data files	Institution	Year	Radar system
A	Data_20180512_01_001 – 004	AWI	2018	MCoRDS 5
A	Data_19990512_01_009 – 010	CReSIS	1999	ICoRDS 2
B	Data_20180512_01_001 – 004	AWI	2018	MCoRDS 5
B	Data_19990523_01_016 – 017	CReSIS	1999	ICoRDS 2
C	Data_20180517_01_002 – 004	AWI	2018	MCoRDS 5
C	Data_20120330_03_008 – 011	CReSIS	2012	MCoRDS 2

Table 2. Operating parameters of the radar systems used for data acquisition. Further details can be found in Gogineni et al. (2001), Byers et al. (2012) and ~~Franke et al. (2021b, in prep.)~~Franke et al. (2021b).

Parameter	ICORDS 2	MCoRDS 2	MCoRDS 5
Bandwidth	141.5–158.5 MHz	180–210 MHz	180–210 MHz
Tx power	200 W	1050 W	6000 W
Waveform	Analogue chirp (SAW)	8 channel chirp (2–3 ~~wave forms~~waveforms)	8 channel chirp (3 ~~wave forms~~waveforms)
Sampling frequency	18.75 MHz	111 MHz	1600 MHz
Transmit channels	1	8	8
Receiving channels	1	15	8
Range resolution	7.6 m	4.3 m	4.3 m

The validation of our modelling results and the correct dating of isochrones requires a reliable depth-age scale. The Greenland Ice Core Chronology 2005 ~~(GICC05 Andersen et al., 2006) to EastGRIP.~~ (GICC05, Vinther et al., 2006; Rasmussen et al., 2006; Andersen is based on annual layer counting in various Greenland ice cores. It has been transferred to GRIP and other deep drilling sites in Greenland by synchronizing the ice cores with each other using horizons of e.g. volcanic origin (Rasmussen et al., 2008; Seierstad et al., 20 . The upper 1,383.84 m of the EastGRIP ice core were drilled between 2015 and 2018, and synchronized with the NorthGRIP ice core in previous work (Mojtabavi et al., 2020).

By 2019, the ice-core drilling progressed down to 2,122.45 m, allowing us to extend the ~~time scale to 49.2~~ existing time scale from 15 ka to 49.9 ka b2k (thousands of years before 2000 CE). ~~We~~ As part of the present study, we identified common isochrones between EastGRIP, NorthGRIP and NEEM to transfer the GICC05 chronology to the ~~EastGRIP record~~part of the EastGRIP record which is not yet synchronized. This involved the same methods applied to NEEM by Rasmussen et al. (2013)

and to the upper 1,383.84 m of EastGRIP by Mojtabavi et al. (2020). The isochrones chosen for synchronization purposes are mainly volcanic eruptions, which are registered as brief spikes in the electrical conductivity measurements (ECM, Hammer, 1980). The search of common ECM spikes was performed manually with a strong focus on finding patterns of similarly spaced eruptions rather than single and isolated events. The Matlab ~~GUI~~ program 'Matchmaker' was used to visualize long data stretches and to evaluate the quality of the match ~~(Rasmussen et al., 2013)~~(Rasmussen et al., 2008). An iterative multi-observer protocol was applied to reduce problems with confirmation bias and to ensure the reproducibility of the match.

A total of ~~262~~ 138 match points were identified between 1,383.84 m and 2,~~106.65~~ 117.77 m, adding to the previously known 381 match points~~found above 1,383.84~~ . The match points between EastGRIP and the other two cores are shown in Fig. 3, representing all the volcanic tie points. The ~~annual-layer-counted~~ GICC05 chronology was transferred to EastGRIP by linear interpolation of depths between the match points. The age of the 1,383.84 m match point was already established to be 14,966 years b2k, which is near the termination of Greenland ~~stadial~~ Stadial 2 (GS-2), with a reported maximum counting error (MCE) of 196 years ~~(Rasmussen et al., 2014)~~(Mojtabavi et al., 2020). The age of the deepest match point was established to be 49,~~200~~ 909 years b2k, just at the end of ~~GS-14~~Greenland Interstadial 14 (GI-14), with an MCE of 2,~~026~~ 066 years.

As in earlier similar work ~~(Rasmussen et al., 2013; Seierstad et al., 2014)~~(e.g Rasmussen et al., 2013; Seierstad et al., 2014) , very few match points were observed in the stadials, most clearly seen in Fig. 3 in the long stadial stages of GS-2 and GS-3. ~~Weakness of volcanic signals across~~ The sparse volcanic signals within stadial periods should not be attributed to a diminished global volcanic activity but rather to increased deposition of alkaline dust that neutralizes volcanic acid, caused by ~~much~~ the prevailing colder and drier climatic conditions (Rasmussen et al., 2013). The largest distance between match points was observed across GS-2 and GS-3 and spans about 162 m of EastGRIP ice.

2.2.1 ~~Isochrone tracing~~

2.3 Tracing and dating of isochrones

~~Electromagnetic waves are sensitive to changes in dielectric permittivity and electrical conductivity. Contrasts in the dielectric properties of ice lead to so-called internal reflection horizons (IRH). In ice sheets, these contrasts typically can have three different origins: The permittivity varies with (1) density contrasts in the uppermost part of the ice column (Robin et al., 1969) or (2) changes in the crystal orientation fabric (Harrison, 1973), and the electrical conductivity of ice is altered by (3) impurity layers such as volcanic deposits (Paren and Robin, 1975). The latter is the most common reflector type below the firn (Millar, 1982; Eisen et , and because it is related to layers deposited over a relatively short period, most internal reflections can be considered isochrones (Siegert, 1999; Hempel et al., 2000). Post-depositional deformation of isochrones provides information on ice-flow dynamics and can be used to reconstruct past and present flow characteristics. We traced IRHs using~~ The depth-age relationship from ice core chronologies can be extended in the lateral plane by tracing and dating of isochrones in RES images. The depth of these isochrones along the EastGRIP flow lines is part of the observed data used to tune the ice flow model parameters in the Monte Carlo inversion. We traced 15 continuous IRHs and one non-continuous reflector along each of the three approximated flow lines with a semi-automatic Matlab program called 'picking tool'. The algorithm is based on calculating the local slope in

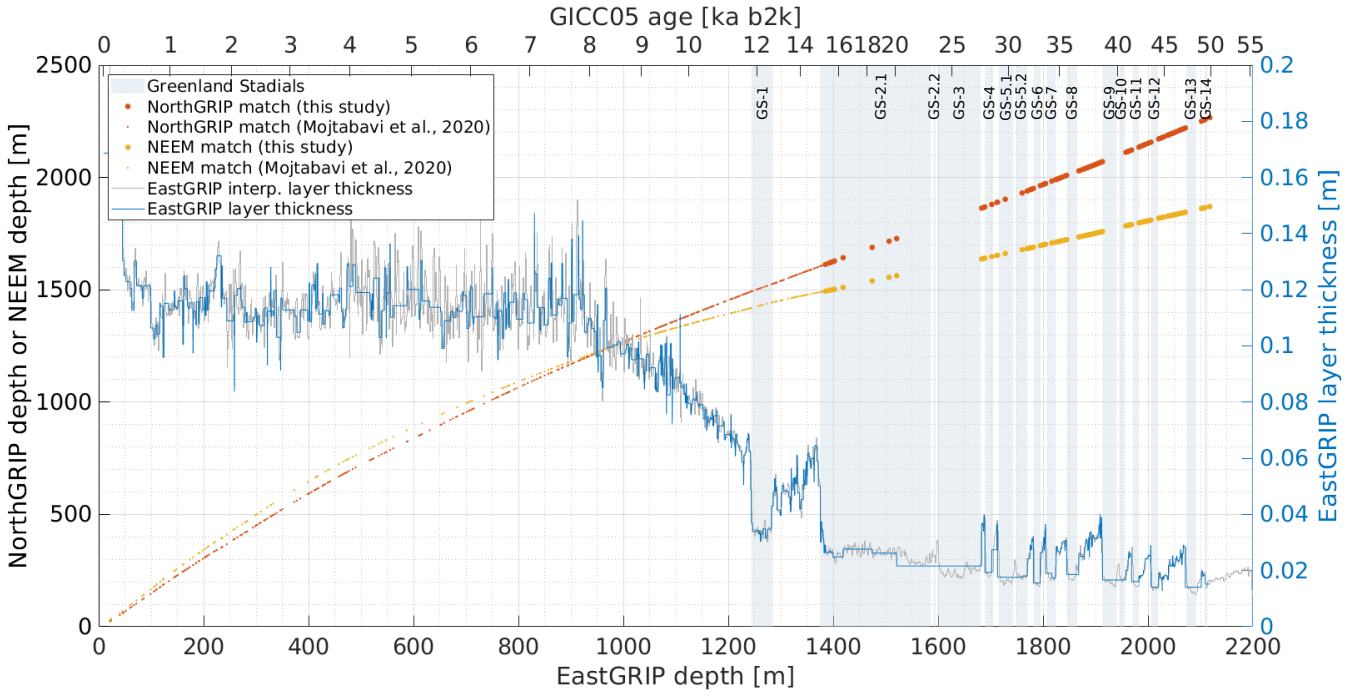

Figure 3. Synchronization between the EastGRIP, NorthGRIP and NEEM ice cores and comparison of match points obtained in this study with earlier results from Mojtabavi et al. (2020). The annual layer thickness of EastGRIP was computed after transferring GICC05 ages by linear interpolation to the EastGRIP ice core. The blue curve shows the annual layer thickness obtained by the match points only. The grey line indicates a high-resolution estimate of annual layer thicknesses at EastGRIP, obtained from the linear interpolation between the EastGRIP–NorthGRIP match points and assigning the interpolated EastGRIP depths to the NorthGRIP ages.

each pixel of the RES image~~by minimizing the variance along a local line segment. Layers~~ , and layers are traced automatically between two user-defined points~~by following~~ . Starting from each of these points the algorithm walks along the steepest slope ~~from both ends and subsequent weighting of~~ towards the other point. Subsequently, the two lines are weighted by distance to ~~the end points~~their starting point and combined to one layer. The number of picks required for thorough tracing depends on the data quality and reflector strength.

The total depth uncertainty ($\tilde{z}_t$) was calculated as ~~:~~

$$\tilde{z}_t = \sqrt{\tilde{z}_p^2 + \tilde{z}_{rr}^2}, \tag{1}$$

where the depth uncertainty introduced during the picking process ~~,~~($\tilde{z}_p$~~,~~) is estimated to be 10 m~~, and $\tilde{z}_{rr}$ is~~ . The uncertainty related to the radar range resolution ($\tilde{z}_{rr}$) of the corresponding RES image ~~and~~ is defined as

$$\tilde{z}_{rr} = \frac{kc}{2B\sqrt{3.15}}, \tag{2}$$

where k is the window widening factor of 1.53, c is the speed of light, B is the radar bandwidth and 3.15 is the dielectric permittivity of ice.

The traced IRHs were dated at both drill sites by assigning the ~~average reflector depth~~ reflector depth at GRIP and EastGRIP to the corresponding time scale. In doing so, local irregularities were smoothed out by averaging the depth over ± 250 ~~m~~ m around the trace closest to the ~~GRIP and EastGRIP sites to the extended GICC05 time scale (Rasmussen et al., 2014; Seierstad et al., 2014; . We extrapolated this~~ ice core location. Because the EastGRIP ice core has not reached the bed yet, we extrapolated the time scale at EastGRIP with ~~2~~ two IRHs observed below the current ~~bore-hole~~ borehole depth to obtain a tentative depth–age relationship between 2,~~106.65~~ 117.77 m and the expected bed depth of 2,~~668.6~~ 668 m.

The total age uncertainty ~~,~~ ($\tilde{a}_t$~~,~~) was estimated by following the approach described in MacGregor et al. (2015), where ~~:~~

$$\tilde{a}_t = \sqrt{\tilde{a}_c^2 + \tilde{a}_{rr}^2 + \tilde{a}_p^2}, \tag{3}$$

takes into account the age uncertainties associated with the time scale ($\tilde{a}_c$, equivalent to 0.5 MCE), the radar range resolution ($\tilde{a}_{rr}$), and the layer picking process ($\tilde{a}_p$). The uncertainties related to the range resolution are estimated with ~~the following formula:~~

$$\tilde{a}_{rr} = \frac{1}{2} \sum |a_c(z \pm \tilde{z}_{rr}) - a_c(z)|, \tag{4}$$

where a_c is the ice-core age from the GICC05 time scale. Similar to Eq. (4), $\tilde{a}_p$ is estimated with

$$\tilde{a}_p = \frac{1}{2} \sum |a_c(z \pm \tilde{z}_p) - a_c(z)|. \tag{5}$$

The chosen isochrones show distinct patterns which could be identified in all RES images and allowed us to trace isochrones across disruptions and data gaps. Comparison of the isochrone depths at the ice-core locations obtained from different RES images permits to assess the quality of the tracing procedure. The high resolution of the radar images recorded in 2018 facilitates isochrone tracing, and the EastGRIP depths obtained from the two different AWI radar profiles agree within 1.5 m. At GRIP, the discrepancy between isochrone depths obtained from three different radar profiles can be up to 30 m, which is slightly above the combined depth uncertainty related to the picking process and the resolution of the RES images. Lower range resolution and signal-to-noise ratio in older RES data introduce bias in isochrone identification, and although distinct isochrones were chosen, a miscorrelation between IRHs recorded by different radar systems can not be entirely excluded. Moreover, the CReSIS profiles do not precisely intersect at GRIP and deviate from each other. The radar traces closest to GRIP are thus found at slightly different locations for the three RES images, which explains the higher discrepancy of radar layer depths.

The isochrone dating was conducted for each profile individually, and the obtained depths, ages and uncertainties were averaged over the three lines (Table 3). The deepest non-continuous layer which could be identified at EastGRIP is found at a depth of 2,360 ± 11 m and is estimated to be 72,400 ± 1,306 years old. The layer depths of the continuously traced IRHs range from 421 ± 11 m to 2,152 ± 11 m at the EastGRIP location, corresponding to ages of 3,498 ± 94 to 51,920 ± 1,240 years b2k. Reflectors 1–9 were deposited during the Holocene. The remaining reflectors are found in ice from the Last Glacial Period from

which reflector 10 and 11 can be attributed to the onset of the Younger Dryas and the Bølling–Allerød. The relation between the GRIP and EastGRIP depths of the traced IRHs fits well with the GICC05 time scale (Mojtabavi et al., 2020; Rasmussen et al., 2014), and the ages obtained from the two drill sites agree within the uncertainties. We note that the layer dating at EastGRIP consistently leads to younger ages than the dating at GRIP, which is a likely consequence of inaccuracies related to the transformation between ice-core and radar depths.

Due to computational reasons, we did not use all 16 layers for the Monte Carlo inversion but picked ten isochrones with approximately equal vertical spacing, and used the EastGRIP ages for our simulation of layer propagation. The layers used for the Monte Carlo simulation are indicated in bold in Table 3 and plotted with a consistent color-code in Fig. 4, Fig. 5 and Fig. 7, representing the corresponding ages.

Table 3. Characteristics of the traced isochrones connecting the GRIP and EastGRIP ice-core sites. Displayed depths and ages are the average over the three flow lines. Depth uncertainties include the uncertainty related to the picking process and to the radar range resolution. Age uncertainties are related to the GICC05 time-scale uncertainties and isochrone depths. Figure 7d illustrates the depth and climatic context of these layers in the EastGRIP ice core, identified with the corresponding layer numbers. The bold layers and the EastGRIP ages were used for the Monte Carlo inversion and are illustrated with a consistent color-code in Fig. 4, Fig. 5 and Fig. 7.

Layer	**GRIP depth [m]**	**EastGRIP depth [m]**	**GRIP age [yrs b2k]**	**EastGRIP age [yrs b2k]**
1	733 ± 13	421 ± 11	3,618 ± 73	3,498 ± 94
2	**795 ± 13**	**471 ± 11**	**4,004 ± 74**	**3,945 ± 95**
3	925 ± 13	573 ± 11	4,885 ± 85	4,805 ± 93
4	**1,217 ± 13**	**838 ± 11**	**7,178 ± 106**	**7,139 ± 95**
5	1,262 ± 13	882 ± **11**	7,575 ± 107	7,531 ± 95
6	**1,347 ± 13**	**968 ± 11**	**8,364 ± 122**	**8,321 ± 110**
7	1,374 ± 13	996 ± 11	8,637 ± 124	8,600 ± 113
8	1,533 ± 13	1,153 ± **11**	10,407 ± 162	10,365 ± 149
9	**1,592 ± 13**	**1,208 ± 11**	**11,209 ± 181**	**11,140 ± 168**
10	1,663 ± 13	1,282 ± 11	12,891 ± 327	12,822 ± 290
11	**1,749 ± 13**	**1,355 ± 11**	**14,612 ± 281**	**14,350 ± 206**
12	**2,039 ± 13**	**1,704 ± 11**	**28,633 ± 840**	**28,522 ± 647**
13	**2,193 ± 13**	**1,903 ± 11**	**38,015 ± 994**	**37,914 ± 793**
14	**2,298 ± 13**	**2,035 ± 11**	**45,463 ± 1,189**	**45,174 ± 1,086**
15	**2,395 ± 13**	**2,152 ± 11**	**52,602 ± 1,360**	**51,920 ± 1,240**
16	-	**2,360 ± 11**	-	**72,400 ± 1,306**

2.4 Ice flow model

A full simulation of ice flow in the catchment area of the NEGIS is a highly under-determined problem (Keisling et al., 2014), lacking geophysical, climatic and ice-core data, some of which will ~~later become available~~ become available in the future. Simpler models do not solve the problem in detail and are thus computationally much cheaper. ~~Limited~~ Hence, limited but still useful information can be obtained from a simplified treatment of ice flow (e.g. Dansgaard and Johnsen, 1969; Dahl-Jensen et al., 2003; Waddington et al., 2007; Christianson et al., 2013; Keisling et al., 2014).

Here, we use a two-dimensional Dansgaard–Johnsen model (Dansgaard and Johnsen, 1969) to simulate the propagation and deformation of internal layers along approximated flow lines between the ice-sheet summit (GRIP) and EastGRIP. The simplicity of the model makes it well suited for the Monte Carlo method due to its few model parameters, the allowance for large time steps, and because it has an analytical solution (Grinsted and Dahl-Jensen, 2002). The model assumes ice incompressibility and a constant vertical strain rate down to the so-called kink height ~~,~~ (h~~,~~) below which the strain rate decreases linearly. Basal sliding and melting are included in the model, and the ice-sheet thickness ~~,~~ (H~~,~~) is assumed to be constant in time.

We consider a coordinate system where the x-axis points along the approximated flow line, the y-axis is horizontal and perpendicular to the flow line, and the z-axis indicates the height above the bed. The horizontal velocities parallel ($u_\parallel$) and perpendicular ($u_\perp$) to the profiles are described by Grinsted and Dahl-Jensen (2002) as:

$$u_\parallel(z) = \begin{cases} u_{\parallel,sur}(x,y)\left[(1-f_{bed})\frac{z}{h} + f_{bed}\right], & z \in [0,h] \\ u_{\parallel,sur}(x,y), & z \in [h,H], \end{cases} \tag{6}$$

$$u_\perp(z) = \begin{cases} u_{\perp,sur}(x,y)\left[(1-f_{bed})\frac{z}{h} + f_{bed}\right], & z \in [0,h] \\ u_{\perp,sur}(x,y), & z \in [h,H] \end{cases} \tag{7}$$

where $u_{\parallel,sur}$ and $u_{\perp,sur}$ are the surface velocities parallel and perpendicular to the profile, and the basal sliding factor ~~, f_B~~ f_{bed}, is the ratio between the ice velocity at the bed and at the surface.

Ice flow in the vicinity of an ice stream is affected by lateral compression and longitudinal extension, in particular across the shear margins of the NEGIS. We thus introduce $\alpha = \frac{\partial u_\parallel}{\partial x} + \frac{\partial u_\perp}{\partial y}$ as the sum of the horizontal strain rates~~, and due~~ . Due to ice incompressibility we can write ~~$\alpha + \frac{\partial w}{\partial z} = 0$~~$\alpha + \frac{\partial \omega}{\partial z} = 0$, where ω symbolizes the vertical velocity. The x and y dependency in Eq. (6 - 7) only relates to the surface velocity, such that α_{sur} represents the horizontal dependency in the equations ~~.~~ and can be calculated from the ice surface velocities.

The vertical velocities ~~(Dansgaard and Johnsen, 1969)~~ (ω) are obtained through integration of the incompressibility relation ~~$w(z) = -\int \alpha dz$:~~ $\omega(z) = -\int \alpha dz$ (Dansgaard and Johnsen, 1969):

$$\omega(z) = \begin{cases} \omega_{bed} - \alpha_{sur}(f_{bed} z + \frac{z^2}{2h}(1-f_{bed})) & z \in [0,h] \\ \omega_{sur} + \alpha_{sur}(H-z) & z \in [h,H]. \end{cases} \tag{8}$$

The boundary conditions ~~at the surface and bedrock are :~~ for the vertical velocity at the bed (ω_{bed}) and surface (ω_{sur}) are

$$\omega_{base bed} = -\lambda_B \dot{b} + f_{B bed} u_{sur} \frac{\partial B}{\partial x} \frac{\partial E_{bed}}{\partial x} \tag{9}$$

$$\omega_{sur} = -\lambda_H \dot{a} + u_{sur} \frac{\partial S}{\partial x} \frac{\partial E_{sur}}{\partial x}, \tag{10}$$

where ~~$\lambda_B \dot{b}$~~ is the positive basal melt rate~~and λ_H~~, $\dot{a}$ is the positive accumulation rate, and E_{bed} and E_{sur} are the bed and surface elevations respectively. From Eq. (8) we derive the following expression for the modelled α_{sur}:

$$\alpha_{sur} = \frac{\omega_{base} - \omega_{sur}}{H - \frac{h}{2}(1 - f_B)},$$

~~and the integration of Eq. (8) yields the isochrone depth–age relationship:~~

$$(H - z) = \frac{-\lambda_H}{\alpha_{sur}}(1 - e^{\alpha_{sur} t}),$$

~~where parameters z and t are the height and age of the isochrones. The unknowns λ_H and α_{sur} are obtained by a curve-fitting function, using at least 5 isochrones younger than 10 at each point along the flow line. The remaining initial flow parameters are approximated as:~~

$$\lambda_{B,0} = e_1 \hat{\mathbf{u}}_{sur}$$

$$f_{B,0} = e_2 \hat{\mathbf{u}}_{sur}$$

$$h_0 = H\left(\tfrac{1}{2} - e_3 \hat{\mathbf{u}}_{sur}\right),$$

$$\alpha_{sur} = \frac{\omega_{bed} - \omega_{sur}}{H - \frac{h}{2}(1 - f_{bed})}. \tag{11}$$

~~with the normalized surface velocities, $\hat{\mathbf{u}}_{sur}$, the ice thickness, H, and the estimated scaling factors $e_1 = 0.03$, $e_2 = 0.8$ and $e_3 = 0.4$. To simulate the propagation of ice particles deposited at the surface of the GrIS, Eq. (6) and Eq. (8) are solved for the past 50 kyr at a time interval of 10 years.~~

2.5 ~~Climate model~~

~~The~~ Following Grinsted and Dahl-Jensen (2002) and Buchardt and Dahl-Jensen (2007), we adjust the accumulation rates and surface velocities ~~are adjusted~~ to the climate conditions of the corresponding time ~~by~~ with a scaling factor $\xi(t)$~~(Johnsen et al., 1995)~~ :

$$\xi(t) = e^{k_2(\delta^{18}O - \delta^{18}O_w) - \frac{1}{2}k_1(\delta^{18}O^2 - \delta^{18}O_w^2)} \kappa_2(\delta^{18}O - \delta^{18}O_w) - \frac{1}{2}\kappa_1(\delta^{18}O^2 - \delta^{18}O_w^2), \tag{12}$$

with $k\kappa_1 = \frac{c_w - c_c}{\delta^{18}O_w - \delta^{18}O_c} \frac{c_w - c_c}{\delta^{18}O_w - \delta^{18}O_c}$, and $k\kappa_2 = c_{ww} - \delta^{18}O_w k_w \kappa_1$.

We use the ~~water~~ oxygen isotope $\delta^{18}O$ record from NorthGRIP (Andersen et al., 2004) due to its high temporal resolution, and $\delta^{18}O_w = -35.2$ ‰ and $\delta^{18}O_c = -42$ ‰ are typical isotope values for warm ~~and cold periods. The unknown parameters c_w and c_c are defined as the relative slopes~~ interstadial and cold stadial periods, respectively. The parameters c_w and c_c determine the sensitivity of the accumulation ~~rates~~ rate with varying $\delta^{18}O$ in warm (c_w) and cold (c_c) periods ~~:~~ and are defined as (Grinsted and Dahl-Jensen, 2002; Buchardt and Dahl-Jensen, 2007):

$$c_w = \frac{1}{\lambda_H}\frac{\partial \lambda_H}{\partial \delta^{18}O}\frac{1}{\dot{a}}\frac{\partial \dot{a}}{\partial \delta^{18}O}\bigg|_{\delta^{18}O=\delta^{18}O_w}, \quad c_c = \frac{1}{\lambda_H}\frac{\partial \lambda_H}{\partial \delta^{18}O}\frac{1}{\dot{a}}\frac{\partial \dot{a}}{\partial \delta^{18}O}\bigg|_{\delta^{18}O=\delta^{18}O_c}. \tag{13}$$

~~which typically assume values between 0 and 2. Like Buchardt and Dahl-Jensen (2007), we find that $c_w = 0.15$ and $c_c = 0.10$ gives a good approximation of the past climate variations.~~

To simulate the propagation of ice particles deposited at the surface of the GrIS, Eq. (6) and Eq. (8) are solved at a time interval of 10 years.

2.5 Monte Carlo sampling

~~The ice-flow parameters λ_H, λ_B~~ The ice flow parameters $\dot{a}$, h, f_{bed}, and $\dot{b}$ are defined for intervals of ~10 km along the flow lines, and form together with the two climate scaling factors, c_c and ~~f_B form the multi-dimensional model space~~ c_w, the model vector $\mathbf{m}$. ~~The observed data , $\mathbf{d}_{obs}$, include the depth of eight selected isochrones of given age~~ This results in a total of 170 (flow line A and B) and 194 (flow line C) model parameters. Each combination of them represents a possible solution to the inverse problem $\mathbf{d} = g(\mathbf{m})$, where $g(\mathbf{m})$ represents the ice flow model described in the previous section. The data vector $\mathbf{d}$ contains the isochrone depths and α_{sur} determined from ~~Eq. (14).The model and data space are related through a non-linear function $\mathbf{d} = g(\mathbf{m})$. The misfit between the observed and modelled data in iteration i is defined as:~~

$$S(\mathbf{m}) = \sum_i \frac{|\mathbf{d}^i_{obs} - \mathbf{d}^i_{model}|}{\sigma^i},$$

~~where σ describes the data uncertainty. The~~ the MEaSUREs Multi-year v1 surface velocities (Joughin et al., 2018) at a resolution of one kilometer.

Like in most geophysical inverse problems, many different combinations of model parameters can explain the observed data equally well within the range of their uncertainties and therefore, a non-unique solution does not exist. Probabilistic inverse methods consider many different models and describe them in terms of their plausibility, rather than finding one possible solution. This makes it particularly well suited for nonlinear problems, where the probability density in the model space typically shows ~~a global maximum surrounded by a large number of local maxima representing other possible solutions (Mosegaard and Tarantola, 1995). The simplest approach to avoid being trapped in one of the local maxima is the global sampling of every point in the model space. However, the amount of model parameters and the non-linear nature of our problem makes this method computationally unfeasible.~~ multiple maxima (Mosegaard and Tarantola, 1995).

Monte Carlo methods ~~allow~~ are based on a random number generator which allows the sampling according to the ~~posterior~~ target probability distribution in ~~a more~~ an efficient way. ~~In the inverse Monte Carlo strategy used here(Mosegaard and Tarantola, 1995)~~

, the current model , $\mathbf{m}_{curr}$, is perturbed by a random walk in The grey box in Fig. 2 illustrates the iterative sampling process of the Metropolis algorithm (Metropolis et al., 1953) used here: Starting from an initial model ($\mathbf{m}_0$), a random walker explores the model space . The perturbation of the ice-flow parameters along the flow lines occurs at intervals of 10 km, which results in a total amount of 168 (flow line A and B) and 188 (flow line C)model parametersproposes new models ($\mathbf{m}_{new}$) which are accepted with a certain probability (P_{accept}). This way of importance sampling avoids unnecessary evaluation of model parameters in low-probability areas (Mosegaard, 1998).

Using the Metropolis algorithm (Metropolis et al., 1953), the perturbed model is accepted with the probability To estimate the initial accumulation rate $\dot{a}_0$, we integrate Eq. (8) (see Appendix A) and obtain the following depth–age relationship

$$P_{accept}(H-z) = \min\frac{L(\mathbf{m}_{pert})}{L(\mathbf{m}_{curr})}, 1\frac{\dot{a}}{\alpha_{sur}}(1-e^{-\alpha_{sur}t}), \tag{14}$$

where the likelihood function is defined as $L(\mathbf{m}) = e^{-S(\mathbf{m})}$. Sampling starts after the burn-in phase, ensuring the statistical independence of model parameters. A threshold regularizes the maximum deviation from the initial model to avoid sampling outside a physically feasible range.

3 Results

2.1 Radar Stratigraphy

Characteristics of the traced isochrones connecting the GRIP and EastGRIP ice-core sites. Displayed depths and ages are the average over the three flow lines. Depth uncertainties include the uncertainty related to the picking process and to the radar range resolution. Age uncertainties are related to the GICC05 time-scale uncertainties and isochrone depths. The bold layers and the EastGRIP ages were used for the Monte Carlo inversion. **Layer GRIP depth m EastGRIP depth m GRIP age yrs b2k EastGRIP age yrs b2k** 1 733 ± 13 421 ± 11 3,618 ± 73 3,498 ± 94 **2 795 ± 13 471 ± 11 4,004 ± 74 3,945 ± 95** 3 925 ± 13 573 ± 11 4t and z represent the isochrone age and height above the bed, respectively. The accumulation rate $\dot{a}$ is determined with a curve-fitting function, using at least 5 isochrones younger than 10 ka at each point along the flow line. The initial kink height (h_0), basal sliding ($f_{bed,0}$) and basal melt rate ($\dot{b}_0$) are scaled with the normalized surface velocity ($\hat{\mathbf{u}}_{sur}$) as follows:

$$h_0 = H\left(\frac{1}{2} - e_1\hat{\mathbf{u}}_{sur}\right) \tag{15}$$

$$f_{bed,0} = e_2\hat{\mathbf{u}}_{sur} \tag{16}$$

$$\dot{b}_0 = e_3\hat{\mathbf{u}}_{sur}, \tag{17}$$

where $e_1 = 0.4$, 885 ± 85 4, 805 ± 93 **4 1,217 ± 13 838 ± 11 7,178 ± 106 7,139 ± 95** $e_2 = 0.8$ and $e_3 = 0.03$, and the initial value for c_w and c_c is assumed to be 0.15 and 0.10 respectively.

5 In each iteration a new model $\mathbf{m}_{new}$ is proposed as

$$\mathbf{m}_{new} = \mathbf{m}_0 + \mathbf{q}\mathbf{A}, \tag{18}$$

where $\mathbf{m}_0$ is the initial model and $\mathbf{A}$ contains the perturbation amplitude of the corresponding model parameter. The vector $\mathbf{q}$ defines the random walk in the multidimensional model space and solely depends on the preceding step. In each iteration, i, one model parameter, j, is randomly selected and perturbed as

$$\mathbf{q}_{i+1}(j) = \mathbf{q}_i(j) + \left(r - \frac{1}{2}\right)\mathbf{p}(j), \tag{19}$$

where r indicates a random number between 0 and 1,262 ± 13 882 ± 11 7,575 ± 107 7,531 ± 95 , and $\mathbf{p}$ regulates the maximum step length per iteration of the selected parameter type. To achieve a good performance of the Monte Carlo algorithm, the values of $\mathbf{A}$ and $\mathbf{p}$ (shown in Table 4) are chosen such that the acceptance ratio for the individual model parameters lies between 25 % and 75 %.

6 1,347 ± 13 968 ± 11 8,364 ± 122 8,321 ± 110 The quality of the proposed model is evaluated by the function $S(\mathbf{m})$ which describes the misfit between the modelled and observed data (see Appendix B). The new model ($\mathbf{m}_{new}$) is accepted with the acceptance probability (Metropolis et al., 1953)

$$P_{accept} = \min\left(\frac{L(\mathbf{m}_{new})}{L(\mathbf{m}_{old})}, 1\right), \tag{20}$$

where $\mathbf{m}_{old}$ is the last accepted model and the likelihood function is defined as $L(\mathbf{m}) = e^{-S(\mathbf{m})}$.

7 1,374 ± 13 996 ± 11 8,637 ± 124 8,600 ± 113 To ensure that parameter sampling is occurring in a physically reasonable range, the a priori probability distribution is assumed to be uniform within the following intervals:

$$\dot{a} \in [\dot{a}_0 - 0.02\mathrm{ma}^{-1}, \dot{a}_0 + 0.02\mathrm{ma}^{-1}] \tag{21}$$

$$h \in [0, H] \tag{22}$$

$$f_{bed} \in [\max(0, f_{bed,0} - 0.3), \min(1, f_{bed,0} + 0.3)] \tag{23}$$

$$\dot{b} \in [0\mathrm{ma}^{-1}, 0.2\mathrm{ma}^{-1}]. \tag{24}$$

The sampling intervals are based on expected values of the corresponding parameter: The initial accumulation rate obtained from the radar stratigraphy is considered to be quite trustworthy but because the local layer approximation is not justified in the survey area (Waddington et al., 2007) we allow the accumulation rate to deviate by 0.02 ma^{-1}. The kink height is limited to the ice sheet thickness, the basal sliding fraction is allowed to deviate by 30 % from the initial model, and the upper limit of the basal melt rate is based on values suggested at EastGRIP by a recent study (Zeising and Humbert, 2021).

8 1,533 ± 13 In their initial phase, Markov Chain Monte Carlo methods move from the starting model towards a high-probability area where the target distribution is sampled. To avoid sampling during this so-called burn-in phase, the first 1,153 ± 11

$\times 10^{6}$ accepted models are discarded. Since only one parameter is perturbed at a time, successive models are highly correlated. To obtain a distribution of independent models, only every 1000th accepted model is saved. The sampling is continued for 6×10^{6} iterations in total.

Table 4. Perturbation amplitude (**A**) and step length (**p**) of the individual model parameters used for the Monte Carlo sampling. The sampling parameters were chosen such that the acceptance ratio of the individual model parameters lies between 25 % and 75 %.

Model parameter	Amplitude (A)	Step length (p)
$\dot{a}$	0.01 ma^{-1}	0.5
$\dot{b}$	0.01 ma^{-1}	1
h	100 m	3
f_{bed}	0.05	2
c_c	0.05	0.5
c_w	0.05	0.5

We traced 15 IRHs connecting the EastGRIP and GRIP drill sites along three approximated flow lines. The chosen isochrones show distinct features which could be identified in all RES images and allowed us to trace isochrones across disruptions and data gaps. Comparison of the isochrone depths at the ice-core locations obtained from different RES images permits to assess the quality of the tracing procedure. The high resolution of the radar images recorded in 2018 facilitates isochrone tracing, and the EastGRIP depths obtained from the two different AWI radar profiles agree within 1.5 . At GRIP, the discrepancy between isochrone depths obtained from three different radar profiles can be up to 30 m, which is slightly above the combined depth uncertainty related to the picking process and the resolution of the RES images. Lower range resolution and signal-to-noise ratio in older RES data introduce bias in isochrone identification, and although distinct isochrones were chosen, a miss-correlation between IRHs recorded by different radar systems can not be entirely excluded. Moreover, the CReSIS profiles do not precisely intersect at GRIP and deviate from each other. The radar traces closest to GRIP are thus found at slightly different locations for the three RES images, which explains the higher discrepancy of radar layer depths. The isochrone dating was conducted for each profile individually, and the obtained depths, ages and uncertainties were averaged over the three lines. The deepest non-continuous layer which could be identified at EastGRIP is found at 2360 m depth and is estimated to be 72,400 years old.The layer depth of the continuously traced IRHs ranges from 421 ± 11 to 2, 152 ± 11 m at the EastGRIP location, corresponding to ages of 3,498 ± 94 to 51,920 ± 1,240 years b2k. Reflectors 1–9 were deposited during the Holocene. The remaining reflectors are found in ice from the Last Glacial Period from which reflector 10 and 11 can be attributed to the onset of the Younger Dryas and the Bølling–Allerød. Due to computational reasons, we did not use all 15 layers for the Monte Carlo inversion but picked eight isochrones with approximately equal vertical spacing (Table 3), and used the EastGRIP ages for our simulation of layer propagation. The relation between the GRIP and EastGRIP depths of the traced IRHs fits well with the GICC05 time scale (Mojtabavi et al., 2020; Rasmussen et al., 2014), and the ages obtained from the two drill sites agree within the uncertainties. We note that the layer dating at EastGRIP consistently leads to younger ages than the dating at GRIP, which is a likely consequence of inaccuracies related to the transformation between ice-core and radar depths.

3 Results

3.1 Model parameters

Due to the highly under-determined nature of our inverse problem mixed-determined nature of the inverse problem addressed in this study, a unique solution of model parameters does not exist. The Monte Carlo sampling results in a number of possible models distributed according to the posterior probability. We Here, we present the mean model parameters with the standard deviations of the posterior probability distribution and emphasize that the histograms of the posterior distributions are important corresponding histograms (Fig. 6) are essential to understand the uncertainties of the parameter considered.

The flow-line characteristics and model parameters for each flow line are summarized in Fig. 4. The radar profiles with the observed and modelled isochrones are displayed as a function of the distance from the EastGRIP boreholeice core location. Particle trajectories were calculated from the simulated velocity field with the mean model parameters and indicate the source area location of ice found at the modelled isochrone depth in the EastGRIP ice core. The isochrones and particle trajectories are illustrated with the same color-code as in Fig. 5 and Fig. 7f, indicating the corresponding age. The horizontal strain rates ($\dot{\varepsilon}_{xx}$, $\dot{\varepsilon}_{yy}$ and $\dot{\varepsilon}_{xy}$) were obtained from the MEaSUREs Multi-year v1 surface velocity components (Joughin et al., 2018) parallel ($u_{\parallel}$) and perpendicular ($u_{\perp}$) to the approximated flow line. The strain rates show mostly low, positive values along the flow lines with the exception of the shear-margin crossing in profile A and B, which is characterized by longitudinal extension and lateral compression.

The central observed features are the following:

1. The accumulation rate decreases with increasing distance from the central ice divide. In flow line A and B, we observe a slight increase in the accumulation rate of it remains almost constant between -220 and -80 km, followed by a drop of about 20 % across the shear margins. In the first ~4–5 % over the shear margin150 km of flow line C, which corresponds to the ice divide, the accumulation rate remains nearly constant, followed by drop of ~ 25–30 % inside the ice stream. a gradual decrease with increasing distance along the profile.

2. The kink height fluctuates around the middle of the ice column in the vicinity of the ice divide ridge and is drawn close closer to the bed in the centre of the profiles, at ~ -200 km. We observe a general increase in the kink height at ~ . Locally very high kink heights are observed in flow line A around -230 km and -150 km, in flow line B at -240 km and -140 km, and at -100 km and note that it remains in the lower part of the ice column at EastGRIPkm in flow line C. In all profiles, h increases substantially at about -60 km.

3. The basal sliding velocity ranges between 0 and 30 50 % of the surface velocity outside the NEGIS and increases to 70–80 % at 60–100 % in the vicinity of EastGRIP.

4. The basal melt rates increase from 0–0.01 at (GRIP) to rate in the beginning of the profiles varies between 0 and 0.03 –0.04 $\mathrm{m a^{-1}}$ at EastGRIP. As for the kink height, flow line A shows strong melt rate fluctuations in the centre of the

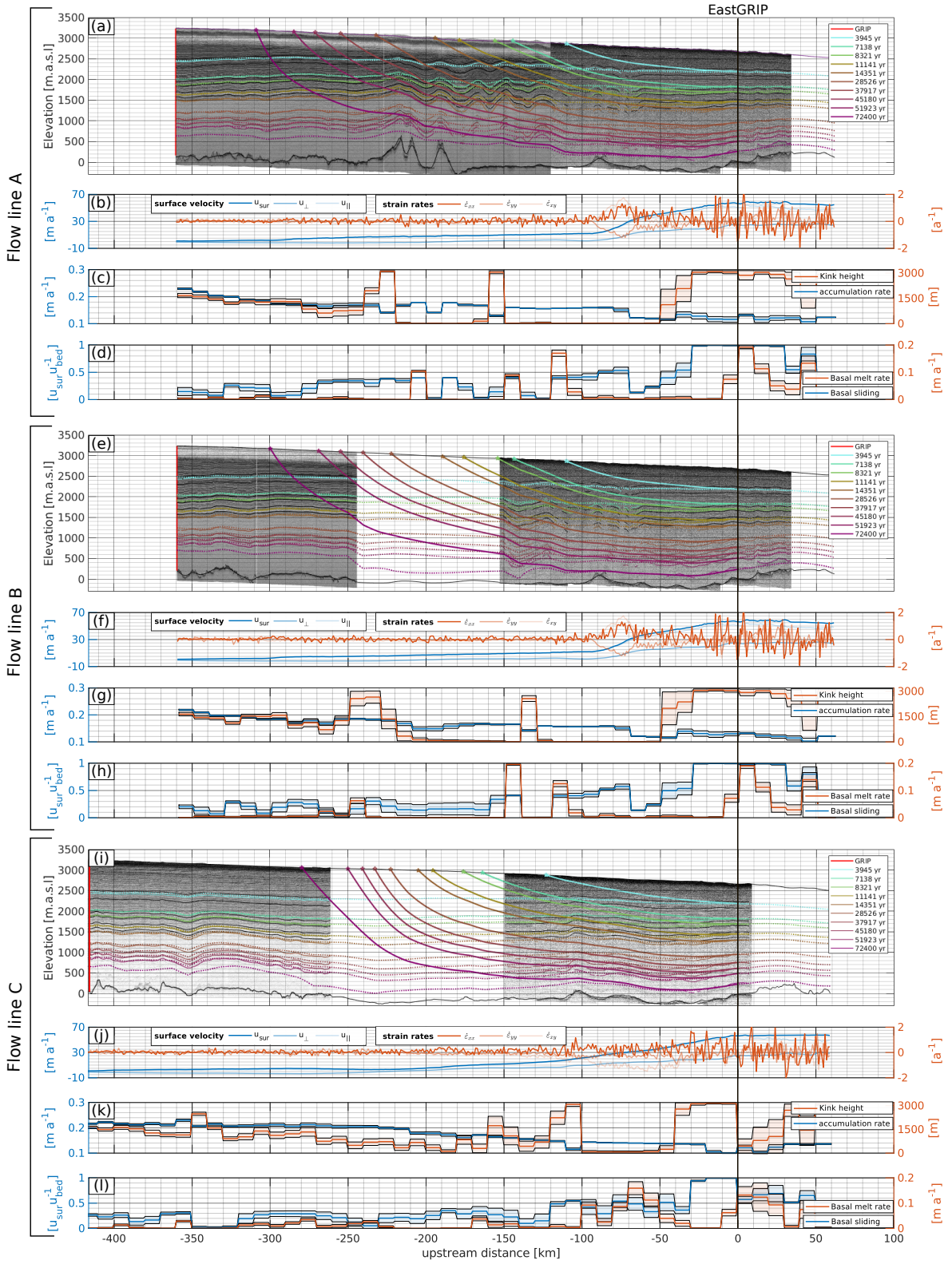
Flow line A
Flow line B
Flow line C
EastGRIP
(a)
(b)
(c)
(d)
(e)
(f)
(g)
(h)
(i)
(j)
(k)
(l)
Elevation [m.a.s.l]
GRIP
3945 yr
7138 yr
8321 yr
11141 yr
14351 yr
28526 yr
37917 yr
45180 yr
51923 yr
72400 yr
surface velocity
strain rates
[m a-1]
[a-1]
Kink height
accumulation rate
[m]
Basal melt rate
Basal sliding
upstream distance [km]

Figure 4. (Previous page.) Flow-line characteristics and model parameters for the approximated flow lines A **(a–d)**, B **(e–h)**, and C **(i–l)**. IRHs were traced (thin solid lines) in RES images and simulated (dashed lines) with a two-dimensional Dansgaard–Johnsen model **(a, e, i)**. From the modelled velocity field, we calculated particle trajectories (thick solid lines) backwards in time to obtain estimates of the source location for specific depths in the EastGRIP ice core. The colors of the lines indicate the age of the isochrones and the respective time of snow deposition and are identical to the color code in Fig. 5 and Fig. 7. The horizontal strain rates at the surface were calculated from the MEaSUREs Multi-year v1 (Joughin et al., 2018) surface velocities **(b, f, j)**. The mean and standard deviations of the sampled model parameters accumulation rate, kink height, basal melt rate and basal sliding **(c, d, g, h, k, l)** were obtained from a Monte Carlo inversion by reducing the misfit between observed and simulated ~~isochrones **(a, e, j)**. From the modelled velocity field we calculated particle trajectories backwards in time to obtain estimates of the source area location of snow deposition for specific depths in the EastGRIP ice core~~data. All panels are aligned at EastGRIP and the x-axis indicates the distance from the borehole location.

profile, some of which are also observed in flow line B. At EastGRIP, basal melt rates between 0.05 and 0.1 ma^{-1} are obtained but higher values of up to 0.2 ma^{-1} are reached further downstream.

3.2 Monte Carlo Performance

The comparison of modelled and observed isochrones (Fig. 5a,c,e) and α_{sur} (supplementary material, Fig. S2) shows a good fit in most parts of the flow lines. However, our model is not able to accurately reproduce strong internal layer undulations which are not related to the ~~bedrock~~ bed topography or the surface conditions, resulting in a larger misfit where such undulations are present (Fig. 5b,d,f). In general, the isochrone misfit tends to be larger for deeper layers. Particularly distinct is the positive misfit at EastGRIP for the deepest layer in all profiles, indicating that the depths of old layers are overestimated. The average isochrone misfit for flow line A, B and C is ~~4.56 %, 4.02 % and 3.16~~ 2.94 %, 2.34 % and 1.49 % of the respective layer depth.

Histograms in Fig. 6 show the sampled ~~posterior~~ probability distribution of model parameters at GRIP and EastGRIP with the corresponding mean and standard deviation displayed on top. Distributions with distinctive single peaks and low standard deviation point towards a good parameter resolution, while multiple maxima ~~and high~~ or large standard deviations indicate that several models are found to be equally likely. The parameter resolution is in general better in the beginning of the profiles, most clearly represented by the narrow distributions in the accumulation rate, basal melt rate and kink height at GRIP. Exponential distributions imply that a parameter reaches regularization boundaries. ~~These are most common in areas containing data gaps and strong isochrone undulations where regularization was necessary to constrain the parameters to a physically plausible range.~~ This is the case for the basal melt rates at GRIP, the kink height and basal sliding factor at EastGRIP, and the accumulation rate in flow lines B and C at EastGRIP. The climate parameter c_w is found to be 0.10 ± 0.005 for all flow lines. The obtained value for parameter c_c is 0.14 ± 0.003 for flow line A and B, and 0.16 ± 0.004 for flow line C respectively. The histograms of c_w and c_c can be found in the supplementary material, Fig. S3.

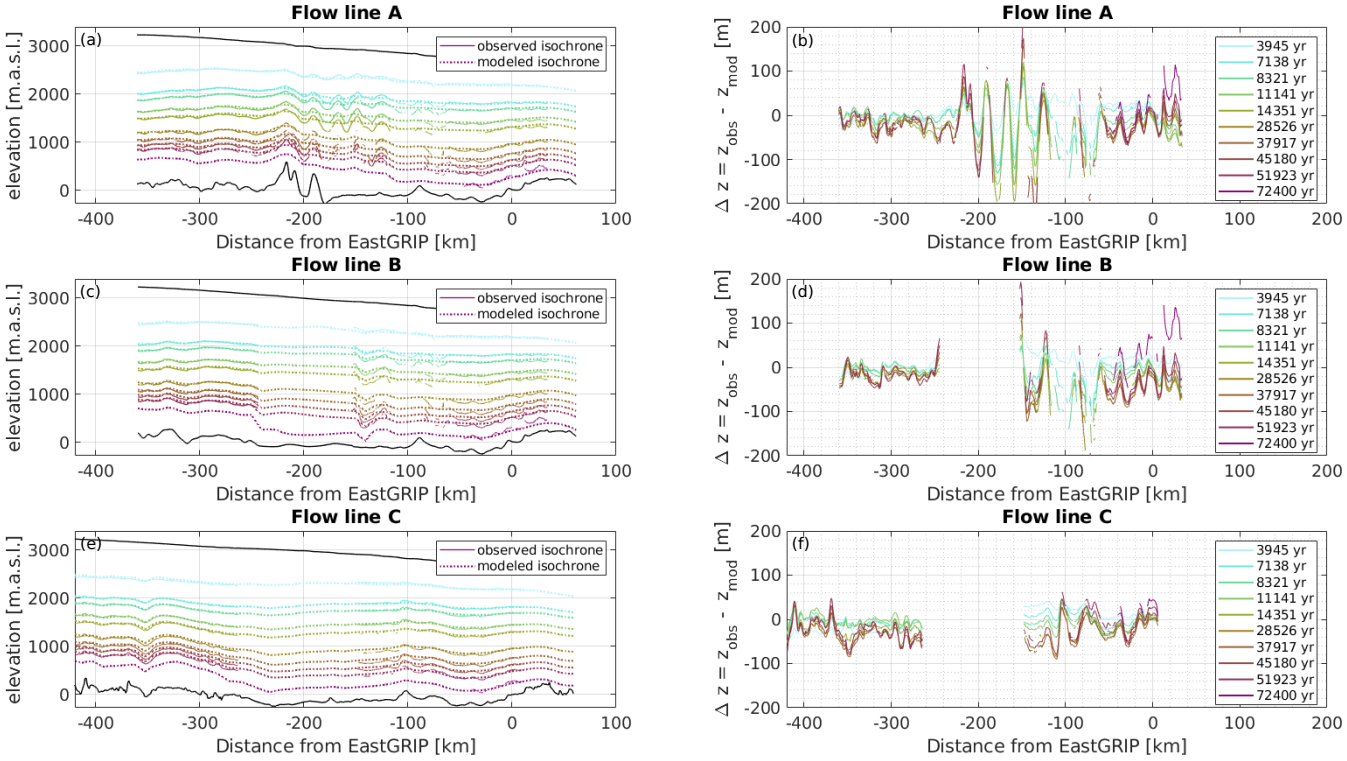

Figure 5. (a, c, e) Modelled and observed isochrones for profile A–C. The model fits the isochrones ~~very~~ well in general but fails to reproduce strong layer undulations over short distances, leading to a larger misfit (panel **b, d, f)** where such undulations are present. ~~**(b, d, f)** Misfit between observed and modelled isochrone height:~~ A positive misfit indicates that the modelled isochrone depth is overestimated which happens in particular for the deepest isochrone towards the end of flow line A and B. As in Fig. 4 and Fig. 7, the color code represents the age of the corresponding isochrone.

3.3 Ice origin and ice-flow history

From the modelled velocity field, we ~~calculated~~ calculate particle trajectories backwards in time (Fig. 4) ~~,~~ which give insight into the source location and flow history of ~~an ice particle~~ ice found at a certain depth in the EastGRIP ice core, and allow us to determine the accumulation rate during its deposition (Fig~~7~~. 7e). Due to the higher velocities in the ice stream, the ~~source area of ice~~ ice source location in the upper 1,600 ~~m~~ m of the ice core lies further upstream for flow line C compared to flow line A and B. For deeper ice, this trend is reversed, as the velocity along flow line C drops below the velocity of line A and B (Fig. 7a). A similar effect manifests itself in the upstream elevation, where higher velocities along flow line C result in higher elevations in the upper part of the ice column, which is compensated by a flatter topographic profile for ice deeper than 1,~~300 m~~ 400 m (Fig. 7b).

From the model-inferred in situ accumulation rates, ~~$\lambda_{H,m}$~~ $\dot{a}_m$, and annual layer thicknesses, λ_m, we calculate the ice-core

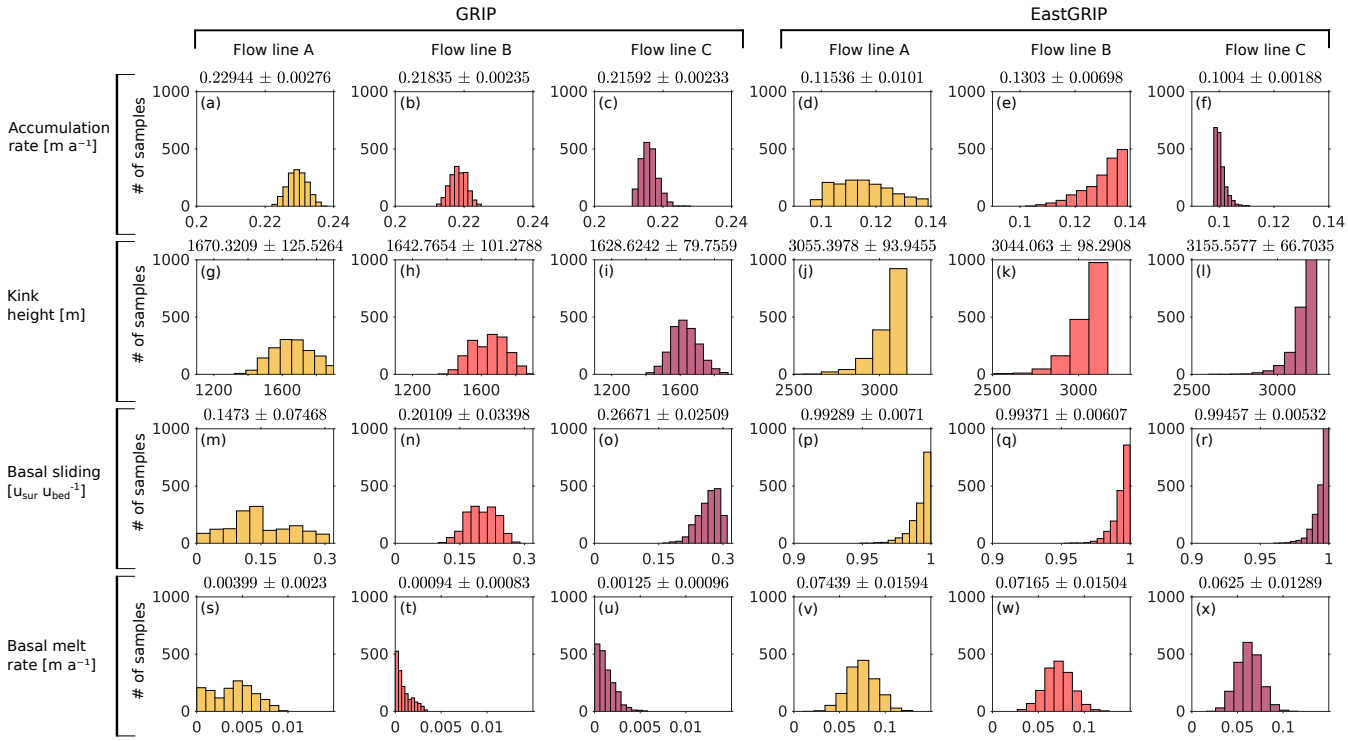

Figure 6. Histograms of the model parameters accumulation rate, basal melt rate, kink height and basal sliding at GRIP and EastGRIP for each flow line. The corresponding means and standard deviations are displayed on top of the histograms.

thinning function γ:

$$\gamma = \frac{\lambda_{H,m} - \lambda_m}{\lambda_{H,m}} \frac{\dot{a}_m - \lambda_m}{\dot{a}_m}. \tag{25}$$

The thinning function increases ~~almost~~ nearly linearly with depth ~~but~~ in the Holocene and shows a considerable ~~lower vertical thinning~~ decrease in the Younger Dryas and enhanced thinning in the Bølling–Allerød. In the glacial part of the ice core, the thinning function fluctuates between interstadials and stadials. The shift between the three lines results from the slightly different depth–age relationship and isochrone misfit obtained from the three profiles. We combine the thinning function with the annual layer thicknesses observed in the EastGRIP ice core, λ_{obs}, to estimate past accumulation rates ~~, $\lambda_{H,c}$:~~ $\dot{a}_{past}$:

$$\lambda_{H,c}\dot{a}_{past} = \frac{\lambda_{obs}}{1-\gamma}. \tag{26}$$

We find that the ~~local~~ accumulation rate at the deposition site increases from ~~the present-day~~ ~0.12 ma^{-1} to a maximum of ~~0.242~~ 0.249 ma^{-1} for ice at ~~913 m depth~~ a depth of 912 m, which was deposited approximately 7,800 years ~~ago~~b2k. We note that the constant annual layer thicknesses observed in the upper 900 ~~m~~ m of the EastGRIP ice core (Mojtabavi et al., 2020) coincides with the spatial pattern of increasing accumulation along the flow line ~~in the upstream area~~with increasing upstream

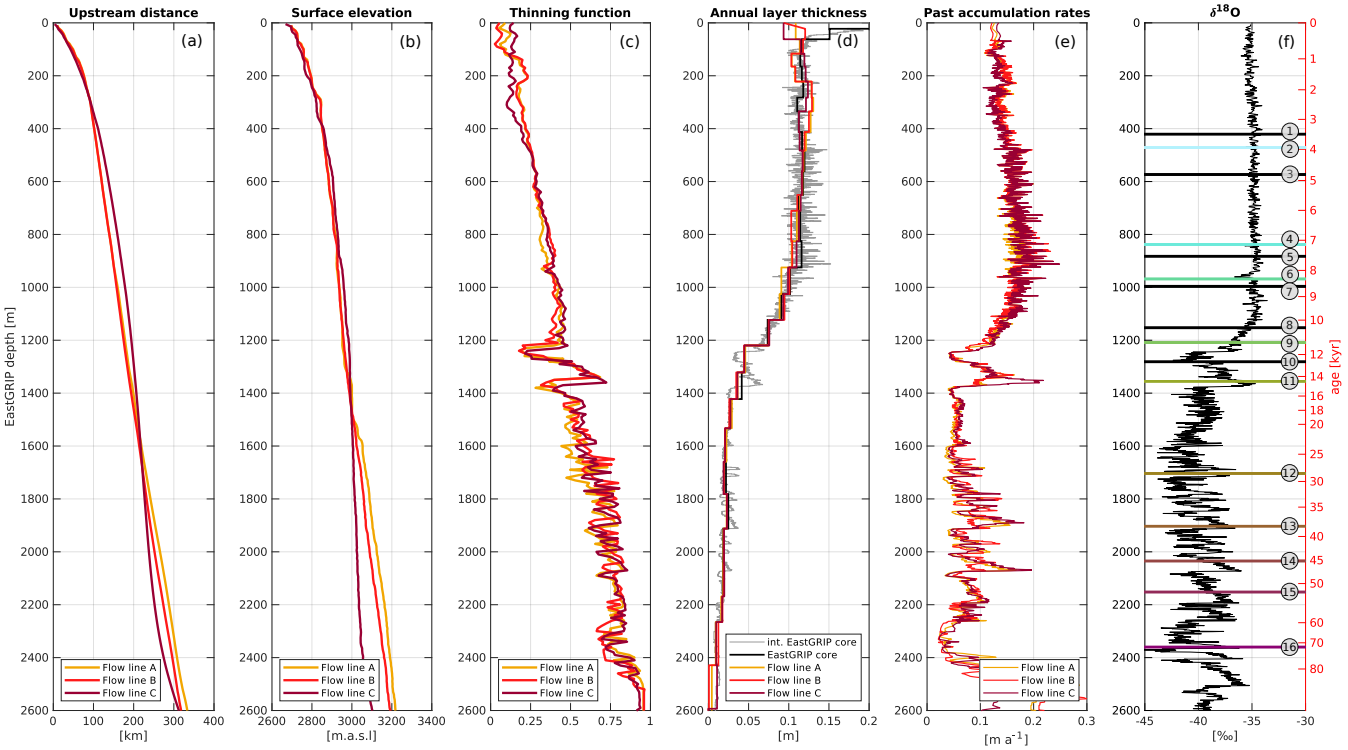

Figure 7. Modelled upstream distance **(a)** and surface elevation **(b)** of the source ~~area~~ location for ice in the EastGRIP ice core. The thinning function **(c)** was calculated from the modelled accumulation rates and annual layer thicknesses **(d)** and was combined with the ~~observed~~ interpolated annual layer thicknesses obsereved in the ice core **(d)** to calculate past accumulation rates in high resolution **(e)**. The $\delta^{18}O$ curve from NorthGRIP **(f)** was scaled to the EastGRIP depths to put the results into a climatic context ~~. Our model can reproduce~~ and the ~~annual layer thicknesses observed in~~ depths of the ~~EastGRIP ice core, indicating that our results~~ traced isochrones from Table 3 are ~~robust. The past accumulation rates at the deposition site increase~~ displayed with ~~depth until 913 m, which compensates for~~ the ~~vertical thinning~~ same color index as in Fig. 4 and ~~produces the constant annual layer thicknesses observed during the past 8 kyr~~Fig. ~~Older ice was deposited under lower accumulation rates due to colder~~ 5 and ~~dryer climatic conditions during~~ labeled with the ~~Last Glacial Period~~corresponding layer number.

Table 5. Essential ~~parameters~~ quantities for upstream corrections for selected depths of the EastGRIP ice core. The upstream distance, elevation and past accumulation rates, ~~$\lambda_{H,past}$~~ $\dot{a}_{past}$, describe the ~~location~~ characteristics of the source ~~area~~ location and the conditions during ice deposition. ~~$\lambda_{H,present}$ describes~~ $\dot{a}_{present}$ represents the corresponding present-day accumulation rates ~~in~~ at the source ~~area~~location. All ~~parameters~~ quantities are averages over the three flow lines and the uncertainties represent the maximum deviation from the mean.

Depth [m]	Age [~~yr b2k~~yr b2k]	Upstream distance [~~km~~km]	Elevation [~~m.a.s.l.~~m.a.s.l.]	Thinning function	~~$\lambda_{H,past}$~~ $\dot{a}_{past}$ [~~m a^{-1}~~ma^{-1}]	~~$\lambda_{H,present}$~~ $\dot{a}_{present}$ [~~m a^{-1}~~ma^{-1}]
100	665	~~52.0~~ 47 ± 3	2,~~759.2~~ 752 ± 10	~~0.12~~ 0.10 ± 0.03	~~0.128~~ 0.12 ± 0.004	~~0.121~~ 0.12 ± 0.015
200	1,553	~~78.7~~ 74 ± 2	2,~~799.2~~ 788 ± 11	~~0.21~~ 0.19 ± 0.08	~~0.143~~ 0.14 ± 0.006	~~0.139~~ 0.14 ± 0.005
300	2,418	~~96.2~~ 92 ± 1	2,~~838.1~~ 837 ± 14	~~0.26~~ 0.16 ± 0.05	~~0.148~~ 0.13 ± 0.005	~~0.143~~ 0.15 ± 0.010
400	3,322	~~108.3~~ 105 ± 7	2,~~858.8~~ 854 ± 6	~~0.22~~ 0.21 ± 0.02	~~0.143~~ 0.14 ± 0.002	~~0.150~~ 0.14 ± 0.031
600	5,037	~~129.7~~ 126 ± 12	2,~~894.4~~ 892 ± 14	0.28 ± 0.00	~~0.160~~ 0.16 ± 0.001	~~0.150~~ 0.16 ± 0.005
800	6,805	~~150.8~~ 146 ± 14	2,~~927.9~~ 920 ± 9	~~0.38~~ 0.35 ± 0.03	~~0.159~~ 0.15 ± 0.005	~~0.154~~ 0.16 ± 0.003
1,000	8,640	~~169.5~~ 165 ± 13	2,~~949.3~~ 944 ± 15	0.42 ± 0.03	~~0.157~~ 0.16 ± 0.004	~~0.165~~ 0.17 ± 0.002
1,200	11,015	~~187.0~~ 183 ± 12	2,~~968.6~~ 965 ± 19	~~0.32~~ 0.41 ± 0.06	~~0.102~~ 0.12 ± 0.010	~~0.171~~ 0.17 ± 0.005
1,400	15,571	~~204.0~~ 200 ± 7	2,~~997.2~~ 993 ± 7	~~0.52~~ 0.46 ± 0.01	~~0.053~~ 0.05 ± 0.001	~~0.161~~ 0.17 ± 0.015
1,600	23,382	~~220.9~~ 217 ± 3	3,~~032.9~~ 027 ± 26	~~0.60~~ 0.52 ± 0.08	~~0.062~~ 0.05 ± 0.007	~~0.172~~ 0.18 ± 0.023
1,800	33,524	~~237.2~~ 234 ± 8	3,~~058.1~~ 054 ± 40	~~0.67~~ 0.72 ± 0.06	~~0.093~~ 0.11 ± 0.028	~~0.179~~ 0.19 ± 0.021
2,000	43,107	~~254.8~~ 252 ± 14	3,~~083.2~~ 079 ± 54	~~0.77~~ 0.73 ± 0.07	~~0.112~~ 0.10 ± 0.019	~~0.173~~ 0.19 ± 0.022
2,200	54,~~487~~ 864	~~271.5~~ 271 ± 19	3,~~108.0~~ 108 ± 73	~~0.77~~ 0.83 ± 0.02	~~0.051~~ 0.07 ± 0.006	~~0.197~~ 0.19 ± 0.030
2,400	~~73,563~~ 75,980	~~286.0~~ 293 ± 18	3,~~125.7~~ 136 ± 80	~~0.78~~ 0.83 ± 0.11	~~0.042~~ 0.08 ± 0.034	~~0.186~~ 0.19 ± 0.023
2,600	~~95,808~~ 94,696	~~297.4~~ 322 ± 12	3,~~142.4~~ 171 ± 67	0.94 ± 0.03	~~0.161~~ 0.18 ± 0.044	~~0.199~~0.20 ± 0.005

distance (Fig. 4c,g,k and Fig. 7d,e). Ice between 900 ~~m~~ m and 1,400 ~~m~~ m is characterized by the transition from the Holocene into the Last Glacial Period with ~~decreasing accumulation rates into~~ decreased accumulation rates in the Younger Dryas and a peak ~~in~~ during the Bølling–Allerød ~~. Older ice was~~(Fig. 7e). The accumulation rate at the deposition site for older ice varies between 0.02 ma^{-1} during stadials and 0.196 ma^{-1} during interstadials. The atmosphere in the glacial period was in general colder and dryer, and hence, accumulation rates were typically lower than today (Cuffey and Clow, 1997). However, due to ~~climatic reasons, deposited under lower accumulation rates between 0.05 in the stadials and 0.14 in interstadials~~the upstream flow effects, the ice from the interstadials could have been deposited under higher accumulation rates than are observed at the EastGRIP site today.

The ~~accumulation-rate variations~~ variations in the past accumulation-rate between the three flow lines ~~are a combination of~~ result from both, the varying along-flow accumulation pattern and different upstream distance of the source ~~area, and the model spread~~ location. The spread between the three models provides important uncertainty estimates. The average ~~spread between the three~~ deviation from the mean accumulation rates is ~~5.2~~ 3.9 % in the Holocene and ~~16.3~~ 20 % in the Last Glacial Period. ~~A~~

~~maximum deviation of 53 % is found~~ The largest spread between the three flow lines is 68 % observed at a depth of 2,~~541~~ 411 m. We remark that, due to missing direct information on the annual layer thicknesses, accumulation rates below the current ~~bore-hole~~ borehole depth of 2,122.45 ~~m~~ m are based on tentative estimates and must be treated accordingly.

4 Discussion

4.1 Isochrone deformation and ice-flow parameters

Deformation of IRHs occurs as a consequence of ~~bedrock~~ bed topography (Robin and Millar, 1982; Jacobel et al., 1993), spatial variations in basal conditions (Weertman, 1976; Whillans, 1976; Whillans and Johnsen, 1983; Catania et al., 2010; Christianson et al., 2013; Leysinger Vieli et al., 2018; Wolovick et al., 2014), spatially varying accumulation rates and corresponding changes in ice-flow geometry (Dansgaard and Johnsen, 1969; Weertman, 1976; Whillans, 1976; Whillans and Johnsen, 1983), and as a consequence of convergent ice flow and ice-stream activity (Bons et al., 2016). Areas of enhanced basal melt rates similarly drag down all the layers above, while variations in accumulation rate, kink height and basal sliding lead to depth-dependent deformation of the isochrones (Keisling et al., 2014).

The accumulation rates of ~~0.22~~0.21–~~0.24~~ .23 ma^{-1} at GRIP and ~0.1–0.13 ma^{-1} at EastGRIP obtained in this study agree ~~well~~ with field observations (Dahl-Jensen et al., 1993; Vallelonga et al., 2014), and the low standard deviations point towards a robust solution. ~~We find that the accumulation rates across the shear margins are 4–5% higher than outside the NEGIS and 25–30% higher than~~ In profiles A and B we observe ~20 % lower accumulation rates inside the ice stream ~~(Fig.4c,g). Despite the low spatial resolution, our findings agree~~ than outside. This agrees to some extent with Riverman et al. (2019), who found 20 % higher accumulation rates ~~across the NEGIS~~ in the shear margins compared to the surrounding~~. High stresses in~~ , although our observations are not confined to the shear margins ~~lead to a faster firn–ice transition and result in topographic depressions, which act as traps for additional drifting snow (Riverman et al., 2019)~~only. Regularization on the accumulation rate was necessary in our model to avoid unrealistic strong fluctuations along the flow lines.

The bed topography and bed lubrication have a considerable effect on ice-flow parameters. Flow over bed undulations affect the elevation of internal layers due to variations in the longitudinal stresses within the ice (Hvidberg et al., 1997) and is often reflected in the surface topography (Cuffey and Paterson, 2010). If the bed is 'sticky', i.e. the basal sliding is small, the ice is compressed along the flow direction while vertically extended (Weertman, 1976), and IRHs are pushed upwards. At a slippery bed, the opposite is the case, resulting in along-flow extension of IRHs which leads to thinning and thus decreasing distance between the IRHs. Keisling et al. (2014) argued that major fold trains existing independently of bed undulations can be explained by variations in the basal sliding conditions. This is, for instance, observed across shear margins, where local, steady state folds are formed as a response to the basal conditions (Keisling et al., 2014; Holschuh et al., 2014). In flow line A, we observe similar 'fold-trains' on a larger scale downstream of a substantial bed undulation (100–200 ~~km~~ km upstream of EastGRIP) ~~. We argue that these~~ and the resulting high basal melt rates and sliding fraction and the low kink heights drag the layers down in the attempt of matching the observed synclines. These strongly deformed isochrones ~~are out-of-the-plane effects since they~~ predominantly appear in parts of the flow lines which deviate from the observed surface velocity direction by more than 15

degrees. ~~Accordingly,~~ We thus argue that they are out-of-the-plane effects and that the isochrones along the ice flow direction are less strongly deformed. Accordingly, it is questionable that the ice in the EastGRIP ice core ~~is presumably not affected by them, and the fact that they~~ has experienced such deformation and that the high local basal melt rates are trustworthy. The fact that these folds are not reproduced very well by the model does therefore not put any constraints on the usefulness of our results for upstream corrections.

The NEGIS differs from other ice streams in Greenland and Antarctica through the lack of clear lateral topographic constraints and high ice-flow velocities reaching exceptionally far inland. The positioning of the shear margins of the NEGIS are most likely strongly interconnected to the subglacial water system and the substrate and morphology of the bed (Christianson et al., 2014; Franke et al., 2021a). The vast amount of ice mass is added to the NEGIS by entering the ice stream through the shear margins (Franke et al., 2021a), resulting in a compressional stress regime perpendicular to the ice stream. The sudden increase in the kink height at around 60 km upstream of EastGRIP pushes the isochrones upwards, similar to the effect of lateral compression. The distribution of available melt-water and a soft, deformable bed facilitate sliding and thus, ice flow acceleration at the NEGIS onset (Christianson et al., 2014). Evidence of a locally enhanced geothermal heat flux and basal ice at the melting point has been presented by e.g. Fahnestock et al. (2001) and MacGregor et al. (2016), and bed lubrication through melt-water production seems to be one of the driving mechanisms for rapid ice flow in the onset region of the NEGIS (Smith-Johnsen et al., 2020b). Our results support these previous findings in the following way: (1) Kink heights close to the ~~bedrock~~ bed in large segments along the flow profiles imply that most shear deformation is happening in the lower part of the ice column or at the ice–bed interface. The increased kink height towards the ends of the profiles can be attributed to the compressional stress regime associated with the addition of ice through the shear margins. (2) Basal melt rates of 0.01 ~~or higher~~ ma^{-1} or higher inside the NEGIS suggest that the basal ice temperatures along the flow lines are at the pressure melting point and enough energy is available to produce melt-water leading to substantial bed lubrication. (3) Basal sliding is present in most segments of the flow lines, suggesting the presence of melt water or deformation of a soft bed. It increases considerably along the flow lines and significantly contributes to the surface velocity at EastGRIP.

While it is commonly accepted that the NEGIS is initiated by a locally enhanced geothermal heat flux (e.g. Fahnestock et al., 2001; Alley et al., 2019), the magnitude thereof and the resulting hydrological conditions of the bed are still highly debated. Previous studies using simple strain-rate models in combination with Holocene radar stratigraphy indicate basal melt rates of 0.1 ma^{-1} or higher in the vicinity of EastGRIP (Fahnestock et al., 2001; Keisling et al., 2014; MacGregor et al., 2016). However, the accuracy of these findings is limited since the local layer approximation (Waddington et al., 2007) is not valid in the surrounding of the NEGIS (Keisling et al., 2014; MacGregor et al., 2016). Remarkably high basal melt rates of 0.16–0.22 ma^{-1} are also suggested by a recent study (Zeising and Humbert, 2021) using an autonomous phase-sensitive radio-echo sounder (ApRES) at EastGRIP. Melt rates in these order of magnitudes would either require an unusual high geothermal heat flux ~~, immensely~~ exceeding the continental background (Fahnestock et al., 2001; Bons et al., 2021) ~~.~~

~~Our results show that the average basal melt rate at EastGRIP over the past 50 kyr was around 0.033 ± 0.009 , and that consistently higher melt rates would cause too much basal mass loss to observe isochrones as old as 72,400 years in the RES images.~~ or an additional heat source (Zeising and Humbert, 2021). Alley et al. (2019) discussed the interactions between the

GrIS and the geothermal anomaly, presumably caused by the passage of Greenland over the Iceland hot spot (Lawver and Müller, 1994), and hypothesized that an exceptionally unsteady and inhomogeneous geothermal heat flux underneath northeast Greenland could arise through perturbations of the mantle stress regime caused by ice-sheet fluctuations. ~~The geothermal heat flux in the onset region of the NEGIS might thus have experienced substantial oscillations in the past, and basal melt rates today could differ from the temporal average over the past 50 kyr.~~

Our results indicate basal melt rates at EastGRIP between 0.05 and 0.1 ma^{-1} but higher values of up to 0.2 ma^{-1} are obtained further downstream. However, the depth of the oldest modelled isochrone tends to be overestimated in this part of the flow lines (Fig. 5), indicating that the basal melt rate is overestimated. Ice flow parameters at a certain location affect the isochrones directly above and further downstream and since EastGRIP is near the end of the radar lines, the information constraining the isochrone depths is limited, leading to overall lower parameter resolution than further upstream.

4.2 EastGRIP source ~~area~~ location and upstream effects

The source region of ice in the EastGRIP ice core extends over ~~~~ more than 300 ~~km~~ km upstream. Holocene ice characterizes the upper 1,244 ~~m~~ m of the ice core and has been advected up to ~~189 km~~197 km. The climatic conditions during the last 8 kyr remained nearly constant with similar accumulation rates as today~~(Table 5)~~. However, due to increasing precipitation towards the central ice divide, ice from the past 8 kyr was deposited under increasingly higher accumulation rates with increasing age ~~.~~ (Table 5). Our results indicate that this upstream effect happens to compensate for the vertical layer thinning and results in the constant annual layer thicknesses observed in the upper 900 ~~m~~ m of the EastGRIP ice core (Mojtabavi et al., 2020). One possible conclusion of this peculiar observation is that snow depositions must have been advected from far enough upstream to allow the compensation of vertical thinning by increased accumulation rates in the source ~~area~~location. This gives reason to the hypothesis that ice flow velocities in the past 8 ~~ka~~ kyr must have been similarly fast as today, and that, therefore, the NEGIS has likely been active during this time. However, we believe that RES images and estimates of present-day accumulation rates along the EastGRIP flow line are necessary to evaluate this hypothesis further.

Between 8 ka b2k and the beginning of the Holocene, accumulation rates decreased at the deposition site due to ~~increasingly~~ progressively colder and dryer climatic conditions ~~,~~ (Cuffey and Clow, 1997) as we go further back in time and transition into the GS-1. The most recent Glacial Period extends from 119,140 to 11,703 years b2k (Walker et al., 2009) and is characterized by Dansgaard–Oeschger events, abrupt transitions between cold stadial and relatively mild interstadial periods (Dansgaard et al., 1982; Johnsen et al., 1992) causing the oscillations in the accumulation rates. Ice from the Last Glacial Period was deposited between ~~189 and 299 km~~ 197 and 332 km upstream from EastGRIP~~under lower accumulation rates than today. The upstream effect of increasing precipitation towards the central ice divide is varying less than in the Holocene, as the change in upstream location per kyr in the record is much smaller.~~ . The basal ice at EastGRIP could be more than 100 ~~ka old and~~ ka old which, according to our models, has been deposited within ~~60 km~~ about 50 km from the ice divide ~~, under conditions which can be expected to be~~ under conditions similar to those at NorthGRIP and GRIP.

Ice ~~which~~ that is entering the NEGIS must somehow ~~propagate through~~ penetrate the shear margin, which is an important characteristic of ice flow in ice streams and might have left an imprint on the crystal fabric and texture of ice extracted at

EastGRIP. Our modelling results along flow line A and B indicate that ice below ~~231 m~~ 239 m in the EastGRIP ice core has passed the shear margin 82 ~~km~~ km from EastGRIP around ~~1,810 years ago~~1.8 ka b2k. Slightly enhanced annual layer thicknesses observed in the ice core at a depth of 230 ~~m~~ m (Fig. 3) seem unrelated to short-term warmer and wetter climate and might thus be an effect of enhanced accumulation across the shear margin, supporting our results. ~~However, flow lines derived from various surface velocity products show quite a large spread with shear-margin crossings between 97 and 152 km from EastGRIP, corresponding to depths between 324 and 826 m in the ice core.~~

Our ~~model shows~~ results show surface elevations at the deposition site which are up to ~~459 m~~ 500 m higher than EastGRIP at the corresponding time. Assuming a normal thermal and pressure gradient, this implies that ice was deposited under up to ~~2.9° C~~ ~3.25°C colder temperatures and up to ~~41 hPa~~ 45 hPa lower pressure than conditions found at the ~~bore-hole~~ borehole location at the time of deposition.

4.3 Limitations

The most ~~important~~ relevant limitation of this study arises from lacking radar data parallel to the flow field in the upstream area of EastGRIP. The approximated flow lines deviate from the present-day surface flow field in some parts by more than 15 degrees, which presumably introduces out-of-the-plane effects. Data gaps encumbered isochrone tracing and restricted the Monte Carlo method due to missing information in those areas. The correlated parameters in the Dansgaard-Johnsen model lead to a vast amount of possible solutions, and the fact that the observed data can be reproduced by our model does not prove the validity of the assumed parameters and the physical interpretation thereof. This becomes for instance evident at the GRIP ice core site, where our results indicate basal sliding of up to 30 %, while the drilling project showed that the bed is frozen at the ice sheet summit (Dahl-Jensen et al., 1998). The apparent basal sliding might thus represent deformation within a soft bed material rather than actual sliding of the ice over the bed. The spatial and formal resolution of the obtained model parameters is limited, in particular towards the end of the profiles due to limited constraining information further downstream.

By introducing the parameter α, our model accounts for lateral compression and extension on a first degree order, but does not capture the full complexity of the flow field across the shear margins. While these play an essential role in the ice-flow dynamics of the NEGIS (Holschuh et al., 2019) and are likely to have left an imprint on the ice found in the EastGRIP ice core, the full simulation of the flow field is not attempted for the purpose of upstream corrections. This would require more complex, 3D numerical ice flow models which are computationally more expensive and thus not suitable for the Monte Carlo method applied here. Moreover, due to the lack of constraining radar data the information gain in terms of the source characteristics and upstream effects of such a 3D model would be modest.

The elevation of the source ~~area~~ location was determined solely from the present-day ice-sheet surface elevation and did not take into account past fluctuations in the ice-sheet thickness. In general, surface elevation changes are relatively minor in the interior areas of central Greenland (Marshall and Cuffey, 2000; Letréguilly et al., 1991). Yet, Vinther et al. (2009) found that the GRIP elevation might have been up to 200 ~~m~~ m higher during the early Holocene than today. We did not take into account changes in the ice thickness due to the large uncertainties which would be introduced, particularly in the Last Glacial Period. Our estimates on the surface elevation of the source ~~area~~ location must thus not be interpreted as absolute values but rather as

relative changes with respect to the surface elevation of ~~EastGRIP~~ the EastGRIP site at the corresponding time.

Lacking data and a general understanding of ice-sheet flow far back in time put up additional constraints, and due to the relatively recent discovery of the NEGIS (Fahnestock et al., 1993), little is known about its evolution in the past. Observations of surface elevation and ice-flow velocities imply that the downstream end of the NEGIS has entered a state of dynamic thinning after at least 25 years of stability (Khan et al., 2014). However, it is not clear for how long the NEGIS has been active and how its catchment geometry changed over time. The assumption of a constant flow field throughout the past ~~50~~ 100 kyr is thus the best currently available, but potentially inaccurate, estimate of the past flow regime.

Our results do not give clear evidence on which of the flow lines gives the best results for upstream corrections. Since the present-day EastGRIP flow line is likely located somewhere between flow line A and C, our results can be interpreted as the outer boundaries and we consider the average over the three flow lines the best estimate for the upstream flow characteristics with the corresponding model spread as uncertainties.

5 Conclusions

We traced isochrones in RES images along three approximated EastGRIP flow lines connecting the EastGRIP and GRIP drill sites. A two-dimensional Dansgaard–Johnsen model was used to simulate the propagation of isochrones along these flow lines. The simplicity of ~~our model allowed~~ the model allowed us to invert for the ice-flow parameters accumulation rate, basal melt rate, kink height and basal sliding fraction~~. The flow parameters obtained from the Monte Carlo inversion give~~ , which give limited but helpful insight into basal properties and ice-flow dynamics and can be used to constrain large-scale ice-sheet models.

On the basis of our modelled two-dimensional velocity field, we calculated particle trajectories backwards in time to determine the deposition site of ice found in the EastGRIP ice core. We present estimates of the upstream distance, surface elevation and accumulation rate at the time and location of ice deposition. This is valuable and necessary information for interpreting ice-core ~~parameters~~measurements, and to separate past climate variability from ~~non-climatic bias~~ non-local imprints introduced by upstream effects. Our studies show that spatially increasing accumulation rates with increasing upstream distance along the flow line ~~in the upstream area~~ are mainly responsible for the constant annual layer thicknesses observed for the last 8 kyr in the EastGRIP ice core.

The lack of radar data along the EastGRIP flow line is the biggest limitation of this study. None of the three simulated flow lines accurately represents the present-day flow field but can be regarded as upper and lower limits framing the upstream effects. The acquisition of further radar data along ~~the NEGIS flow line~~ NEGIS flow lines in the future would thus provide more accurate and valuable insights into the flow history of the EastGRIP ice and the NEGIS.

Data availability. The CReSIS radio-echo-sounding images used for isochrone tracing are publicly available on https://data.cresis.ku.edu/. The RES data recorded by AWI will be available by Jansen et al. (2020) and described by (Franke et al., 2021b). The extended EastGRIP

time scale, our derived and approximated flow lines and an extended version of Table 5 will be available on https://www.iceandclimate.nbi.ku.dk/data/ and in the supplementary material to this paper.

Notation

z	height above bed
x, y	direction parallel, perpendicular to the flow profile
$\tilde{z}_t, \tilde{z}_p, \tilde{z}_{rr}$	total, picking related, radar related isochrone depth uncertainty
k	radar window widening factor
c	speed of light
B	radar band width
$\tilde{a}_t, \tilde{a}_p, \tilde{a}_{rr}, \tilde{a}_c$	total, picking related, radar related, ice core related age uncertainty
a_c	ice core age
$u_\parallel(z), u_{\parallel,sur}$	flow-line-parallel velocity at depth, at the surface
$u_\perp(z), u_{\perp,sur}$	flow-line-perpendicular velocity at depth, at the surface
$\hat{\mathbf{u}}_{sur}$	normalized surface velocity along the flow line
$\omega(z), \omega_{sur}, \omega_{bed}$	vertical velocity at depth, at the surface, at the bed
$f_{bed}, f_{bed,0}$	basal sliding fraction, initial basal sliding fraction
h, h_0	kink height, initial kink height
H	ice thickness
α	sum of horizontal strain rates $\dot{\varepsilon}_{xx} + \dot{\varepsilon}_{yy}$
E_{bed}	bed elevation above sea level
E_{sur}	surface elevation above sea level
$\dot{a}, \dot{a}_m, \dot{a}_c, \dot{a}_{past}, \dot{a}_{present}$	positive accumulation rate, Monte Carlo inferred, ice core inferred, past, present
$\dot{b}$	positive basal melt rate
$e_{1,2,3}$	scaling factors for initial model parameters
$\xi(t)$	climatic scaling factor
t	time b2k
c_c, c_w	sensitivity of accumulation rates in cold stadial, warm interstadial periods
$\partial^{18}O_c, \partial^{18}O_w$	typical isotope values for cold stadial, warm interstadial periods
$\mathbf{d}, \mathbf{d}_{obs}, \mathbf{d}_{model}$	data space, observed, modelled data
$\mathbf{m}, \mathbf{m}_{old}, \mathbf{m}_{new}$	model space, old, new model
σ_z, σ_α	data uncertainty on isochrone depth, α_{sur}
P_{accept}	acceptance probability
L	likelihood function
S	misfit function
$\lambda, \lambda_m, \lambda_{obs}$	annual layer thickness, modelled, observed
γ	ice core thinning function
$\dot{\varepsilon}_{xx}, \dot{\varepsilon}_{yy}, \dot{\varepsilon}_{xy}$	horizontal strain rates

Appendix A: Derivation of Eq. (14)

The vertical velocity in the upper part of the ice column is given by

$$w(z) = w_{sur} + \alpha_{sur}(H - z) = \frac{dz}{dt}, \qquad z \in [h, H]. \tag{A1}$$

Assuming that the surface slope is close to zero, $\frac{\partial E_{sur}}{\partial x} \simeq 0$, integration of Eq. (A1) with separation of variables results in:

$$\int_z^H \frac{1}{-\dot{a} + \alpha_{sur}(H - z)} dz = \int_t^0 1 dt \tag{A2}$$

$$\left[-\frac{1}{\alpha_{sur}} \ln(\alpha_{sur}(H - z) - \dot{a}) \right]_z^H = [t]_t^0 \tag{A3}$$

$$-\frac{1}{\alpha_{sur}} \left(\ln(-\dot{a}) - \ln(\alpha_{sur}(H - z) - \dot{a}) \right) = -t \tag{A4}$$

$$(H - z) = \frac{\dot{a}}{\alpha_{sur}} (1 - e^{-\alpha_{sur} t}) \tag{A5}$$

Appendix B: Definition of the misfit function S(m)

The function $S(\mathbf{m})$ is defined as:

$$S(\mathbf{m}) = \frac{1}{2} \left(\frac{1}{10} \sum_{l=1}^{10} \left(\frac{1}{n_z} \sum_{n=1}^{n_z} \mathbf{M}_z^2 \right) + \frac{1}{n_\alpha} \sum_{n=1}^{n_\alpha} \mathbf{M}_\alpha^2 \right) * 1000, \tag{B1}$$

where l runs through the 10 layers, n_z and n_α are the number of observed isochrone depths and α_{sur} along the flow lines, and

$$\mathbf{M}_z = \frac{\mathbf{d}_{mod,z} - \mathbf{d}_{obs,z}}{\sigma_z} \quad \text{and} \quad \mathbf{M}_\alpha = \frac{\mathbf{d}_{mod,\alpha} - \mathbf{d}_{obs,\alpha}}{\sigma_\alpha}. \tag{B2}$$

The matrix $\mathbf{M}_z$ describes the misfit between modelled ($\mathbf{d}_{mod,z}$) and observed ($\mathbf{d}_{obs,z}$) isochrones, and the vector $\mathbf{M}_\alpha$ is the misfit between modelled ($\mathbf{d}_{mod,\alpha}$) and observed ($\mathbf{d}_{obs,\alpha}$) α_{sur}. The data uncertainty σ_z is the maximum depth uncertainty of 13 m, and the uncertainty on α_{sur} (σ_α) is assumed to be 10 % of the maximum observed α_{sur}. The factor 1000 is a tuning parameter to ensure the acceptance ratio remains between 25 % and 75 %.

Author contributions. DDJ and TAG designed and carried out the study. AG developed the code used for isochrone tracing. AG and CSH derived the EastGRIP flow lines. DJ was co-investigator for the AWI radar survey and acquired the data in the field. SF processed the radar data obtained during the EGRIP-NOR-2018 AWI flight campaign. SOR, GS and TAG synchronized the EastGRIP ice core with NorthGRIP and NEEM and extended the time scale to the current drill depth. TAG prepared the manuscript with the contribution of all co-authors.

Competing interests. The authors declare that they have no conflict of interest.

Acknowledgements. This work was supported by the Villum Investigator Project IceFlow (NR. 16572). EastGRIP is directed and organized by the Centre for Ice and Climate at the Niels Bohr Institute, University of Copenhagen. It is supported by funding agencies and institutions in Denmark (A. P. Møller Foundation, University of Copenhagen), USA (US National Science Foundation, Office of Polar Programs), Germany (Alfred Wegener Institute, Helmholtz Centre for Polar and Marine Research), Japan (National Institute of Polar Research and Arctic Challenge for Sustainability), Norway (University of Bergen and Trond Mohn Foundation), Switzerland (Swiss National Science Foundation), France (French Polar Institute Paul-Emile Victor, Institute for Geosciences and Environmental research), Canada (University of Manitoba) and China (Chinese Academy of Sciences and Beijing Normal University). We acknowledge the use of data and data products from CReSIS generated with support from the University of Kansas, NASA Operation IceBridge grant NNX16AH54G, NSF grants ACI-1443054, OPP-1739003, and IIS-1838230, Lilly Endowment Incorporated, and Indiana METACyt Initiative. We also acknowledge the use of the CReSIS toolbox from CReSIS generated with support from the University of Kansas, NASA Operation IceBridge grant NNX16AH54G, and NSF grants ACI-1443054, OPP-1739003, and IIS-1838230. We thank the crew of the research aircraft Polar 6 and system Engineer Lukas Kandora for their work during the AWI flight campaign 2018 and express our gratitude to John Paden and Tobias Binder, who helped with the data acquisition during the AWI survey. Sune Olander Rasmussen and Giulia Sinnl gratefully acknowledge the Carlsberg Foundation for supporting the project ChronoClimate. This research was enabled in part by computing facilities and support provided by WestGrid (www.westgrid.ca) and Compute Canada Calcul Canada (www.computecanada.ca). The scientific colour maps 'hawaii' and '~~vik~~roma' (Crameri, 2020) are used in this study to prevent visual distortion of the data and exclusion of readers with ~~colourvision~~ colourvision deficiencies (Crameri et al., 2020).

References

Ageta, Y., Azuma, N., Fujii, Y., Fujino, K., Fujita, S., Furukawa, T., Hondoh, T., Kameda, T., Kamiyama, K., Katagiri, K., Kawada, K., Kawamura, T., Kobayashi, S., Mae, S., Maeno, H., Miyahara, T., Motoyama, H., Nakayama, Y., Naruse, R., Nishio, F., Saitoh, K., Saitoh, T., Shimbori, K., Shiraiwa, T., Shoji, H., Takahashi, A., Takahashi, S., Tanaka, Y., Yokoyama, K., and Watanabe, O.: Deep ice-core drilling at Dome Fuji and glaciological studies in east Dronning Maud Land, Antarctica, Annals of Glaciology, 27, 333–337, https://doi.org/10.3189/1998aog27-1-333-337, 1998.

Aizen, V. B., Aizen, E. M., Joswiak, D. R., Fujita, K., Takeuchi, N., and Nikitin, S. A.: Climatic and atmospheric circulation pattern variability from ice-core isotope/geochemistry records (Altai, Tien Shan and Tibet), Annals of Glaciology, 43, 49–60, https://doi.org/10.3189/172756406781812078, 2006.

Alley, R. B., Bolzan, J. F., and Whillans, I. M.: Polar firn densification and grain growth, Annals of Glaciology, 3, 7–11, https://doi.org/doi:10.3189/S0260305500002433, 1982.

Alley, R. B., Meese, D. A., Shuman, C. A., Gow, A. J., Taylor, K. C., Grootes, P. M., White, J. W., Ram, M., Waddington, E. D., Mayewski, P. A., and Zielinski, G. A.: Abrupt increase in Greenland snow accumulation at the end of the Younger Dryas event, Nature, 362, 527–529, https://doi.org/10.1038/362527a0, 1993.

Alley, R. B., Pollard, D., Parizek, B. R., Anandakrishnan, S., Pourpoint, M., Stevens, N. T., MacGregor, J. A., Christianson, K., Muto, A., and Holschuh, N.: Possible Role for Tectonics in the Evolving Stability of the Greenland Ice Sheet, Journal of Geophysical Research: Earth Surface, 124, 97–115, https://doi.org/10.1029/2018JF004714, 2019.

Andersen, J. K., Kusk, A., Boncori, J. P. M., Hvidberg, C. S., and Grinsted, A.: Improved ice velocity measurements with Sentinel-1 TOPS interferometry, Remote Sensing, 12, 1–22, https://doi.org/10.3390/rs12122014, 2020.

Andersen, K. K., Azuma, N., Barnola, J. M., Bigler, M., Biscaye, P., Caillon, N., Chappellaz, J., Clausen, H. B., Dahl-Jensen, D., Fischer, H., Flückiger, J., Fritzsche, D., Fujii, Y., Goto-Azuma, K., Grønvold, K., Gundestrup, N. S., Hansson, M., Huber, C., Hvidberg, C. S., Johnsen, S. J., Jonsell, U., Jouzel, J., Kipfstuhl, S., Landais, A., Leuenberger, M., Lorrain, R., Masson-Delmotte, V., Miller, H., Motoyama, H., Narita, H., Popp, T., Rasmussen, S. O., Raynaud, D., Rothlisberger, R., Ruth, U., Samyn, D., Schwander, J., Shoji, H., Siggard-Andersen, M. L., Steffensen, J. P., Stocker, T., Sveinbjörnsdóttir, A. E., Svensson, A., Takata, M., Tison, J. L., Thorsteinsson, T., Watanabe, O., Wilhelms, F., and White, J. W.: High-resolution record of Northern Hemisphere climate extending into the last interglacial period, Nature, 431, 147–151, https://doi.org/10.1038/nature02805, 2004.

Andersen, K. K., Svensson, A., Johnsen, S. J., Rasmussen, S. O., Bigler, M., Röthlisberger, R., Ruth, U., Siggaard-Andersen, M. L., Peder Steffensen, J., Dahl-Jensen, D., Vinther, B. M., and Clausen, H. B.: The Greenland Ice Core Chronology 2005, 15-42 ka. Part 1: constructing the time scale, Quaternary Science Reviews, 25, 3246–3257, https://doi.org/10.1016/j.quascirev.2006.08.002, 2006.

Aschwanden, A., Fahnestock, M. A., and Truffer, M.: Complex Greenland outlet glacier flow captured, Nature communications, 7, 1–8, https://doi.org/10.1038/ncomms10524, 2016.

Barbante, C., Barnola, J. M., Becagli, S., Beer, J., Bigler, M., Boutron, C., Blunier, T., Castellano, E., Cattani, O., Chappellaz, J., Dahl-Jensen, D., Debret, M., Delmonte, B., Dick, D., Falourd, S., Faria, S., Federer, U., Fischer, H., Freitag, J., Frenzel, A., Fritzsche, D., Fundel, F., Gabrielli, P., Gaspari, V., Gersonde, R., Graf, W., Grigoriev, D., Hamann, I., Hansson, M., Hoffmann, G., Hutterli, M. A., Huybrechts, P., Isaksson, E., Johnsen, S., Jouzel, J., Kaczmarska, M., Karlin, T., Kaufmann, P., Kipfstuhl, S., Kohno, M., Lambert, F., Lambrecht, A., Lambrecht, A., Landais, A., Lawer, G., Leuenberger, M., Littot, G., Loulergue, L., Lüthi, D., Maggi, V., Marino, F., Masson-Delmotte, V., Meyer, H., Miller, H., Mulvaney, R., Narcisi, B., Oerlemans, J., Oerter, H., Parrenin, F., Petit, J. R., Raisbeck, G., Raynaud, D.,

Röthlisberger, R., Ruth, U., Rybak, O., Severi, M., Schmitt, J., Schwander, J., Siegenthaler, U., Siggaard-Andersen, M. L., Spahni, R., Steffensen, J. P., Stenni, B., Stocker, T. F., Tison, J. L., Traversi, R., Udisti, R., Valero-Delgado, F., Van Den Broeke, M. R., Van De Wal, R. S., Wagenbach, D., Wegner, A., Weiler, K., Wilhelms, F., Winther, J. G., and Wolff, E.: One-to-one coupling of glacial climate variability in Greenland and Antarctica, Nature, 444, 195–198, https://doi.org/10.1038/nature05301, 2006.

Beyer, S., Kleiner, T., Aizinger, V., Rückamp, M., and Humbert, A.: A confined–unconfined aquifer model for subglacial hydrology and its application to the Northeast Greenland Ice Stream, The Cryosphere, 12, 3931–3947, https://doi.org/10.5194/tc-12-3931-2018, 2018.

Bons, P. D., Jansen, D., Mundel, F., Bauer, C. C., Binder, T., Eisen, O., Jessell, M. W., Llorens, M. G., Steinbach, F., Steinhage, D., and Weikusat, I.: Converging flow and anisotropy cause large-scale folding in Greenland's ice sheet, Nature Communications, 7, 1–6, https://doi.org/10.1038/ncomms11427, 2016.

Bons, P. D., de Riese, T., Franke, S., Llorens, M.-G., Sachau, T., Stoll, N., Weikusat, I., Westhoff, J., and Zhang, Y.: Comment on "Exceptionally high heat flux needed to sustain the Northeast Greenland Ice Stream" by Smith-Johnsen et al. (2020), The Cryosphere, 15, 2251–2254, https://doi.org/10.5194/tc-15-2251-2021, 2021.

Buchardt, S. L. and Dahl-Jensen, D.: Estimating the basal melt rate at NorthGRIP using a Monte Carlo technique, Annals of Glaciology, 45, 137–142, https://doi.org/10.3189/172756407782282435, 2007.

Burgess, E. W., Forster, R. R., Box, J. E., Mosley-Thompson, E., Bromwich, D. H., Bales, R. C., and Smith, L. C.: A spatially calibrated model of annual accumulation rate on the Greenland Ice Sheet (1958-2007), Journal of Geophysical Research: Earth Surface, 115, 1–14, https://doi.org/10.1029/2009JF001293, 2010.

Byers, K. J., Harish, A. R., Seguin, S. A., Leuschen, C. J., Rodriguez-Morales, F., Paden, J., Arnold, E. J., and Hale, R. D.: A modified wideband dipole antenna for an airborne VHF ice-penetrating radar, IEEE Transactions on Instrumentation and Measurement, 61, 1435–1444, https://doi.org/10.1109/TIM.2011.2181780, 2012.

Catania, G., Hulbe, C., and Conway, H.: Grounding-line basal melt rates determined using radar-derived internal stratigraphy, Journal of Glaciology, 56, 545–554, https://doi.org/10.3189/002214310792447842, 2010.

Christianson, K., Parizek, B. R., Alley, R. B., Horgan, H. J., Jacobel, R. W., Anandakrishnan, S., Keisling, B. A., Craig, B. D., and Muto, A.: Ice sheet grounding zone stabilization due to till compaction, Geophysical Research Letters, 40, 5406–5411, https://doi.org/10.1002/2013GL057447, 2013.

Christianson, K., Peters, L. E., Alley, R. B., Anandakrishnan, S., Jacobel, R. W., Riverman, K. L., Muto, A., and Keisling, B. A.: Dilatant till facilitates ice-stream flow in northeast Greenland, Earth and Planetary Science Letters, 401, 57–69, https://doi.org/10.1016/j.epsl.2014.05.060, 2014.

Crameri, F.: Scientific colour maps, https://doi.org/10.5281/zenodo.4153113, 2020.

Crameri, F., Shephard, G. E., and Heron, P. J.: The misuse of colour in science communication, Nature Communications, 11, 1–10, https://doi.org/10.1038/s41467-020-19160-7, 2020.

CReSIS: Radar Depth Sounder Data Products, Lawrence, Kansas, USA, http://data.cresis.ku.edu/, 2020.

Cuffey, K. M. and Clow, G. D.: Temperature, accumulation, and ice sheet elevation in central Greenland through the last deglacial transition, Journal of Geophysical Research: Oceans, 102, 26 383–26 396, https://doi.org/10.1029/96JC03981, 1997.

Cuffey, K. M. and Paterson, W. S. B.: The physics of glaciers, Butterworth-Heinemann/Elsevier, Amsterdam, 4. ed. edn., 2010.

Dahl-Jensen, D., Johnsen, S. J., Hammer, C. U., Clausen, H. B., and Jouzel, J.: Past Accumulation rates derived from observed annual layers in the GRIP ice core from Summit, Central Greenland, Ice in the Climate System, 112, 517–532, https://doi.org/10.1007/978-3-642-85016-5_29, 1993.

Dahl-Jensen, D., Mosegaard, K., Gundestrup, N., Clow, G. D., Johnsen, S. J., Hansen, A. W., and Balling, N.: Past temperatures directly from the Greenland ice sheet, Science, 282, 268–271, https://doi.org/10.1126/science.282.5387.268, 1998.

Dahl-Jensen, D., Gundestrup, N., Gogineni, S. P., and Miller, H.: Basal melt at NorthGRIP modeled from borehole, ice-core and radio-echo sounder observations, Annals of Glaciology, 37, 207–212, https://doi.org/10.3189/172756403781815492, 2003.

Dansgaard, W.: Stable isotopes in precipitation, Tellus, 16, 436–468, https://doi.org/10.3402/tellusa.v16i4.8993, 1964.

Dansgaard, W. and Johnsen, S. J.: A Flow Model and a Time Scale for the Ice Core from Camp Century, Greenland, Journal of Glaciology, 8, 215–223, https://doi.org/10.3189/s0022143000031208, 1969.

Dansgaard, W., Clausen, H. B., Gundestrup, N., Hammer, C. U., Johnsen, S. F., Kristinsdottir, P. M., and Reeh, N.: A new Greenland deep ice core, Science, 218, 1273–1277, https://doi.org/10.1126/science.218.4579.1273, 1982.

Delaygue, G. and Bard, E.: An Antarctic view of Beryllium-10 and solar activity for the past millennium, Climate Dynamics, 36, 2201–2218, https://doi.org/10.1007/s00382-010-0795-1, 2011.

Eicher, O., Baumgartner, M., Schilt, A., Schmitt, J., Schwander, J., Stocker, T. F., and Fischer, H.: Climatic and insolation control on the high-resolution total air content in the NGRIP ice core, Climate of the Past, 12, 1979–1993, https://doi.org/10.5194/cp-12-1979-2016, 2016.

Eisen, O., Wilhelms, F., Steinhage, D., and Schwander, J.: Improved method to determine radio-echo sounding reflector depths from ice-core profiles of permittivity and conductivity, Journal of Glaciology, 52, 299–310, https://doi.org/10.3189/172756506781828674, 2006.

Fahnestock, M., Bindschadler, R., Kwok, R., and Jezek, K.: Greenland Ice Sheet surface properties and ice dynamics from ERS-1 SAR imagery, https://doi.org/10.1126/science.262.5139.1530, 1993.

Fahnestock, M., Abdalati, W., Joughin, I., Brozena, J., and Gogineni, P.: High geothermal heat flow, basal melt, and the origin of rapid ice flow in central Greenland, Science, 294, 2338–2342, https://doi.org/10.1126/science.1065370, 2001.

Finkel, R. C. and Nishiizumi, K.: Beryllium 10 concentrations in the Greenland Ice Sheet Project 2 ice core from 3-40 ka, Journal of Geophysical Research: Oceans, 102, 26 699–26 706, https://doi.org/10.1029/97JC01282, 1997.

Franke, S., Jansen, D., Binder, T., Dörr, N., Helm, V., Paden, J., Steinhage, D., and Eisen, O.: Bed topography and subglacial landforms in the onset region of the Northeast Greenland Ice Stream, Annals of Glaciology, 61, 143–153, https://doi.org/10.1017/aog.2020.12, 2020.

Franke, S., Jansen, D., Beyer, S., Neckel, N., Binder, T., Paden, J., and Eisen, O.: Complex basal conditions and their influence on ice flow at the onset of the Northeast Greenland Ice Stream, Journal of Geophysical Research: Earth Surface, 126, https://doi.org/10.1029/2020jf005689, 2021a.

Franke, S., Jansen, D., Binder, T., Paden, J. D., Dörr, N., Gerber, T., Miller, H., Dahl-Jensen, D., Helm, V., Steinhage, D., Weikusat, I., Wilhelms, F., and Eisen, O.: Airborne ultra-wideband radar sounding over the shear margins and along flow lines at the onset region of the Northeast Greenland Ice Stream, Earth System Science Data Discussions, 2021, 1–24, https://doi.org/10.5194/essd-2021-91, 2021b.

Fudge, T. J., Steig, E. J., Markle, B. R., Schoenemann, S. W., Ding, Q., Taylor, K. C., McConnell, J. R., Brook, E. J., Sowers, T., White, J. W., Alley, R. B., Cheng, H., Clow, G. D., Cole-Dai, J., Conway, H., Cuffey, K. M., Edwards, J. S., Lawrence Edwards, R., Edwards, R., Fegyveresi, J. M., Ferris, D., Fitzpatrick, J. J., Johnson, J., Hargreaves, G., Lee, J. E., Maselli, O. J., Mason, W., McGwire, K. C., Mitchell, L. E., Mortensen, N., Neff, P., Orsi, A. J., Popp, T. J., Schauer, A. J., Severinghaus, J. P., Sigl, M., Spencer, M. K., Vaughn, B. H., Voigt, D. E., Waddington, E. D., Wang, X., and Wong, G. J.: Onset of deglacial warming in West Antarctica driven by local orbital forcing, Nature, 500, 440–444, https://doi.org/10.1038/nature12376, 2013.

Fudge, T. J., Lilien, D. A., Koutnik, M., Conway, H., Stevens, C. M., Waddington, E. D., Steig, E. J., Schauer, A. J., and Holschuh, N.: Advection and non-climate impacts on the South Pole Ice Core, Climate of the Past, 16, 819–832, https://doi.org/10.5194/cp-16-819-2020, 2020.

Gardner, A. S., Fahnestock, M. A., and Scambos, T. A.: ITS_LIVE Regional Glacier and Ice Sheet Surface Velocities, https://doi.org/10.5067/6II6VW8LLWJ7, 2020.

Gogineni, S., Tammana, D., Braaten, D., Leuschen, C., Akins, T., Legarsky, J., Kanagaratnam, P., Stiles, J., Allen, C., and Jezek, K.: Coherent radar ice thickness measurements over the Greenland ice sheet, Journal of Geophysical Research Atmospheres, 106, 33 761–33 772, https://doi.org/10.1029/2001JD900183, 2001.

Gow, A. J., Ueda, H. T., and Garfield, D. E.: Antarctic ice sheet: Preliminary results of first core hole to bedrock, Science, 161, 1011–1013, https://doi.org/10.1126/science.161.3845.1011, 1968.

Greene, C. A., Gwyther, D. E., and Blankenship, D. D.: Antarctic Mapping Tools for Matlab, Computers & Geosciences, 104, 151–157, https://doi.org/10.1016/j.cageo.2016.08.003, 2017.

Grinsted, A. and Dahl-Jensen, D.: A Monte Carlo-tuned model of the flow in the NorthGRIP area, Annals of Glaciology, 35, 527–530, https://doi.org/10.3189/172756402781817130, 2002.

Hammer, C. U.: Acidity of Polar Ice Cores in Relation to Absolute Dating, Past Volcanism, and Radio–Echoes, Journal of Glaciology, 25, 359–372, https://doi.org/10.3189/s0022143000015227, 1980.

Harrison, C. H.: Radio Echo Sounding of Horizontal Layers in Ice, Journal of Glaciology, 12, 383–397, https://doi.org/10.3189/s0022143000031804, 1973.

Hempel, L., Thyssen, F., Gundestrup, N., Clausen, H. B., and Miller, H.: A comparison of radio-echo sounding data and electrical conductivity of the GRIP ice core, Journal of Glaciology, 46, 369–374, https://doi.org/10.3189/172756500781833070, 2000.

Herron, M. M. and Langway, C. C.: Firn densification: an empirical model., Journal of Glaciology, 25, 373–385, https://doi.org/10.1017/S0022143000015239, 1980.

Holschuh, N., Christianson, K., and Anandakrishnan, S.: Power loss in dipping internal reflectors, imaged using ice-penetrating radar, Annals of Glaciology, 55, 49–56, https://doi.org/10.3189/2014AoG67A005, 2014.

Holschuh, N., Lilien, D. A., and Christianson, K.: Thermal Weakening, Convergent Flow, and Vertical Heat Transport in the Northeast Greenland Ice Stream Shear Margins, Geophysical Research Letters, 46, 8184–8193, https://doi.org/10.1029/2019GL083436, 2019.

Hvidberg, C. S., Keller, K., Gundestrup, N. S., Tscherning, C. C., and Forsberg, R.: Mass balance and surface movement of the Greenland ice sheet at summit, Central Greenland, Geophysical Research Letters, 24, 2307–2310, https://doi.org/10.1029/97GL02280, 1997.

Hvidberg, C. S., Grinsted, A., Dahl-Jensen, D., Khan, S. A., Kusk, A., Andersen, J. K., Neckel, N., Solgaard, A., Karlsson, N. B., Kjær, H. A., et al.: Surface velocity of the Northeast Greenland Ice Stream (NEGIS): assessment of interior velocities derived from satellite data by GPS, The Cryosphere, 14, 3487–3502, https://doi.org/10.5194/tc-14-3487-2020, 2020.

Jacobel, R. W., Gades, A. M., Gottschling, D. L., Hodge, S. M., and Wright, D. L.: Interpretation of radar-detected internal layer folding in West Antarctic ice streams, Journal of Glaciology, 39, 528–537, https://doi.org/10.1017/s0022143000016427, 1993.

Jansen, D., Franke, S., Binder, T., Paden, J. D., Steinhage, D., Helm, V., and Eisen, O.: AWI UWB radar data along ice flow upstream of the EGRIP drill site at the onset region of the Northeast Greenland Ice Stream, https://doi.org/10.1594/PANGAEA.914258, 2020.

Johnsen, S. J., Clausen, H. B., Dansgaard, W., Fuhrer, K., Gundestrup, N., Hammer, C. U., Iversen, P., Jouzel, J., Stauffer, B., and Steffensen, J. P.: Irregular glacial interstadials recorded in a new Greenland ice core, Nature, 359, 311–313, https://doi.org/10.1038/359311a0, 1992.

Johnsen, S. J., Dahl-Jensen, D., Dansgaard, W., and Gundestrup, N.: Greenland palaeotemperatures derived from GRIP bore hole temperature and ice core isotope profiles, Tellus, Series B, 47 B, 624–629, https://doi.org/10.3402/tellusb.v47i5.16077, 1995.

Joughin, I., Fahnestock, M., MacAyeal, D., Bamber, J. L., and Gogineni, P.: Observation and analysis of ice flow in the largest Greenland ice stream, Journal of Geophysical Research: Atmospheres, 106, 34 021–34 034, https://doi.org/10.1029/2001JD900087, 2001.

Joughin, I., Smith, B. E., and Howat, I. M.: A complete map of Greenland ice velocity derived from satellite data collected over 20 years, Journal of Glaciology, 64, 1–11, https://doi.org/10.1017/jog.2017.73, 2018.

Jouzel, J., Alley, R. B., Cuffey, K. M., Dansgaard, W., Grootes, P., Hoffmann, G., Johnsen, S. J., Koster, R. D., Peel, D., Shuman, C. A., Stievenard, M., Stuiver, M., and White, J.: Validity of the temperature reconstruction from water isotopes in ice cores, Journal of Geophysical Research: Oceans, 102, 26 471–26 487, https://doi.org/10.1029/97JC01283, 1997.

Keisling, B. A., Christianson, K., Alley, R. B., Peters, L. E., Christian, J. E., Anandakrishnan, S., Riverman, K. L., Muto, A., and Jacobel, R. W.: Basal conditions and ice dynamics inferred from radar-derived internal stratigraphy of the northeast Greenland ice stream, Annals of Glaciology, 55, 127–137, https://doi.org/10.3189/2014AoG67A090, 2014.

Khan, S. A., Kjær, K. H., Bevis, M., Bamber, J. L., Wahr, J., Kjeldsen, K. K., Bjørk, A. A., Korsgaard, N. J., Stearns, L. A., Van Den Broeke, M. R., Liu, L., Larsen, N. K., and Muresan, I. S.: Sustained mass loss of the northeast Greenland ice sheet triggered by regional warming, Nature Climate Change, 4, 292–299, https://doi.org/10.1038/nclimate2161, 2014.

Koutnik, M. R., Fudge, T., Conway, H., Waddington, E. D., Neumann, T. A., Cuffey, K. M., Buizert, C., and Taylor, K. C.: Holocene accumulation and ice flow near the West Antarctic Ice Sheet Divide ice core site, Journal of Geophysical Research: Earth Surface, 121, 907–924, https://doi.org/10.1002/2015JF003668, 2016.

Lawver, L. A. and Müller, R. D.: Iceland hotspot track, Geology, 22, 311–314, https://doi.org/10.1130/0091-7613(1994)022<0311:IHT>2.3.CO;2, 1994.

Letréguilly, A., Reeh, N., and Huybrechts, P.: The Greenland ice sheet through the last glacial-interglacial cycle, Palaeogeography, Palaeoclimatology, Palaeoecology, 90, 385–394, https://doi.org/10.1016/S0031-0182(12)80037-X, 1991.

Leysinger Vieli, G. J., Martín, C., Hindmarsh, R. C., and Lüthi, M. P.: Basal freeze-on generates complex ice-sheet stratigraphy, Nature Communications, 9, 1–13, https://doi.org/10.1038/s41467-018-07083-3, 2018.

Lorius, C., Jouzel, J., Ritz, C., Merlivat, L., Barkov, N. I., Korotkevich, Y. S., and Kotlyakov, V. M.: A 150,000-year climatic record from Antarctic ice, Nature, 316, 591–596, https://doi.org/10.1038/316591a0, 1985.

MacGregor, J. A., Fahnestock, M. A., Catania, G. A., Paden, J. D., Prasad Gogineni, S., Young, S. K., Rybarski, S. C., Mabrey, A. N., Wagman, B. M., and Morlighem, M.: Radiostratigraphy and age structure of the Greenland Ice Sheet, Journal of Geophysical Research: Earth Surface, 120, 212–241, https://doi.org/10.1002/2014JF003215, 2015.

MacGregor, J. A., Fahnestock, M. A., Catania, G. A., Aschwanden, A., Clow, G. D., Colgan, W. T., Gogineni, S. P., Morlighem, M., Nowicki, S. M., Paden, J. D., Price, S. F., and Seroussi, H.: A synthesis of the basal thermal state of the Greenland Ice Sheet, Journal of Geophysical Research: Earth Surface, 121, 1328–1350, https://doi.org/10.1002/2015JF003803, 2016.

Marcott, S. A., Bauska, T. K., Buizert, C., Steig, E. J., Rosen, J. L., Cuffey, K. M., Fudge, T. J., Severinghaus, J. P., Ahn, J., Kalk, M. L., McConnell, J. R., Sowers, T., Taylor, K. C., White, J. W., and Brook, E. J.: Centennial-scale changes in the global carbon cycle during the last deglaciation, Nature, 514, 616–619, https://doi.org/10.1038/nature13799, 2014.

Marshall, S. J. and Cuffey, K. M.: Peregrinations of the Greenland Ice Sheet divide in the last glacial cycle: Implications for central Greenland ice cores, Earth and Planetary Science Letters, 179, 73–90, https://doi.org/10.1016/S0012-821X(00)00108-4, 2000.

Meese, D. A., Gow, A. J., Alley, R. B., Zielinski, G. A., Grootes, P. M., Ram, M., Taylor, K. C., Mayewski, P. A., and Bolzan, J. F.: The Greenland Ice Sheet Project 2 depth-age scale: Methods and results, Journal of Geophysical Research: Oceans, 102, 26 411–26 423, https://doi.org/10.1029/97JC00269, 1997.

Metropolis, N., Rosenbluth, A. W., Rosenbluth, M. N., Teller, A. H., and Teller, E.: Equation of state calculations by fast computing machines, The Journal of Chemical Physics, 21, 1087–1092, https://doi.org/10.1063/1.1699114, 1953.

Millar, D.: Acidity levels in ice sheets from radio echo-sounding, Annals of Glaciology, 3, 199–203, https://doi.org/10.3189/S0260305500002779, 1982.

Mojtabavi, S., Wilhelms, F., Cook, E., Davies, S., Sinnl, G., Skov Jensen, M., Dahl-Jensen, D., Svensson, A., Vinther, B., Kipfstuhl, S., Jones, G., Karlsson, N., Faria, S. H., Gkinis, V., Kjær, H., Erhardt, T., Berben, S., Nisancioglu, K., Koldtoft, I., and Rasmussen, S. O.: A first chronology for the East GReenland Ice-core Project (EGRIP) over the Holocene and last glacial termination, Climate of the Past, 16, 2359–2380, https://doi.org/10.5194/cp-2019-143, 2020.

Morlighem, M., Williams, C. N., Rignot, E., An, L., Arndt, J. E., Bamber, J. L., Catania, G., Chauché, N., Dowdeswell, J. A., Dorschel, B., Fenty, I., Hogan, K., Howat, I., Hubbard, A., Jakobsson, M., Jordan, T. M., Kjeldsen, K. K., Millan, R., Mayer, L., Mouginot, J., Noël, B. P., O'Cofaigh, C., Palmer, S., Rysgaard, S., Seroussi, H., Siegert, M. J., Slabon, P., Straneo, F., van den Broeke, M. R., Weinrebe, W., Wood, M., and Zinglersen, K. B.: BedMachine v3: Complete Bed Topography and Ocean Bathymetry Mapping of Greenland From Multibeam Echo Sounding Combined With Mass Conservation, Geophysical Research Letters, 44, 11,051–11,061, https://doi.org/10.1002/2017GL074954, 2017.

Mosegaard, K.: Resolution analysis of general inverse problems through inverse Monte Carlo sampling, Inverse problems, 14, 405, 1998.

Mosegaard, K. and Tarantola, A.: Monte Carlo sampling of solutions to inverse problems, Journal of Geophysical Research, 100, 12 431 –12 447, https://doi.org/10.1029/94jb03097, 1995.

Mottram, R., Simonsen, S. B., Svendsen, S. H., Barletta, V. R., Sørensen, L. S., Nagler, T., Wuite, J., Groh, A., Horwath, M., Rosier, J., Solgaard, A., Hvidberg, C. S., and Forsberg, R.: An integrated view of greenland ice sheet mass changes based on models and satellite observations, Remote Sensing, 11, 1–26, https://doi.org/10.3390/rs11121407, 2019.

NEEM Community members, Dahl-Jensen, D., Albert, M., Aldahan, A., Azuma, N., Balslev-Clausen, D., Baumgartner, M., Berggren, A.-M., Bigler, M., Binder, T., Blunier, T., Bourgeois, J. C., Brook, E. J., Chuchardt, S. L., Buizert, C., Capron, E., Chappellaz, J., Chung, J., Clausen, H. B., Cvijanovic, I., Davis, S. M., Ditlevsen, P., Eicher, O., Fischer, H., Fisher, D. A., Fleet, L., Gfeller, G., Gkinis, V., Gogineni, S., Goto-Azuma, K., Grinsted, A., Gudlaugsdottir, H., Guillevic, M., Hansen, S. B., Hansson, M., Hirabayashi, M., Hong, S., Hur, S. D., Huybrechts, P., Hvidberg, C., Iizuka, Y., Jenk, T., Johnsen, S. J., Jones, T. R., Jouzel, J., Karlsson, N. B., Kawamura, K., Keegan, K., Kettner, E., Kipfstuhl, S., Kjær, H. A., Koutnik, M., Kuramoto, T., Köhler, P., Laepple, T., Landais, A., Langen, P., Larsen, L. B., Leuenberger, D., Leuenberger, M., Leuschen, C., Li, J., Lippenkov, V., Mirtinerie, P., Maselli, O. J., Masson-Delmotte, V., McConnel, J. R., Miller, H., Mini, O., Miyamoto, A., Montagnat-Rentier, M., Mulvaney, R., Muscheler, R., Orsi, A. J., Paden, J., Panton, C., Pattyn, F., Petit, J. R., Pol, K., Popp, T., Possnert, G., Prié, F., Prokopiou, M., Quique, A., Rasmussen, S. O., Raynaud, D., Ren, J., Reutenauer, C., Ritz, C., Roeckeman, T., Rosen, J. L., Rubino, M., Rybak, O., Samyn, D., Sapart, C. J., Schilt, A., Schmidt, A., Schwander, J., Schüpbach, S., Seierstad, I., Severinghaus, J. P., Sheldon, S., Simonsen, S. B., Sjolte, J., Solgaard, A. M., Sowers, T., Sperlich, P., Steen-Larsen, H. C., Steffen, K., Steffensen, J. P., Steinhage, D., Stocker, T., Stowasser, C., Sturevik, A. S., Sturges, B., Sveinbjörnsdottir, A., Svensson, A., Tison, J.-L., Uetake, J., Vallelonga, P., van de Wal, R. S. W., van der Wel, G., Vaughn, B. H., Vinther, B., Waddington, E., Wegner, A., Weikusat, I., White, J. W. C., Wilhelms, F., Winstrup, M., Witrant, E., Wolff, E., Xiao, C., and Zheng, J.: Eemian interglacial reconstructed from a Greenland folded ice core, Nature, 493, 489–494, https://doi.org/10.1038/nature11789, 2013.

Paren, J. G. and Robin, G. d. Q.: Internal Reflections in Polar Ice Sheets, Journal of Glaciology, 14, 251–259, https://doi.org/10.3189/s0022143000021730, 1975.

Parrenin, F., Barnola, J. M., Beer, J., Blunier, T., Castellano, E., Chappellaz, J., Dreyfus, G., Fischer, H., Fujita, S., Jouzel, J., Kawamura, K., Lemieux-Dudon, B., Loulergue, L., Masson-Delmotte, V., Narcisi, B., Petit, J. R., Raisbeck, G., Raynaud, D., Ruth, U., Schwander, J., Severi, M., Spahni, R., Steffensen, J. P., Svensson, A., Udisti, R., Waelbroeck, C., and Wolff, E.: The EDC3 chronology for the EPICA Dome C ice core, Climate of the Past, 3, 485–497, https://doi.org/10.5194/cp-3-485-2007, 2007.

Petit, J. R., Raynaud, D., Basile, I., Chappellaz, J., Davisk, M., Ritz, C., Delmotte, M., Legrand, M., Lorius, C., Pe, L., and Saltzmank, E.: Climate and atmospheric history of the past 420,000 years from the Vostok ice core , Antarctica, Nature, 399, 429–436, https://doi.org/10.1038/20859, 1999.

Porter, C., Morin, P., Howat, I., Noh, M.-J., Bates, B., Peterman, K., Keesey, S., Schlenk, M., Gardiner, J., Tomko, K., Willis, M., Kelleher, C., Cloutier, M., Husby, E., Foga, S., Nakamura, H., Platson, M., Wethington, Michael, J., Williamson, C., Bauer, G., Enos, J., Arnold, G., Kramer, W., Becker, P., Doshi, A., D'Souza, C., Cummens, P., Laurier, F., and Bojesen, M.: ArcticDEM, https://doi.org/10.7910/DVN/OHHUKH, 2018.

Raisbeck, G. M., Yiou, F., Jouzel, J., and Stocker, T. F.: Direct north-south synchronization of abrupt climate change record in ice cores using Beryllium 10, Climate of the Past, 3, 541–547, https://doi.org/10.5194/cp-3-541-2007, 2007.

Rasmussen, S., Seierstad, I., Andersen, K. K., Bigler, M., Dahl-Jensen, D., and Johnsen, S.: Synchronization of the NGRIP, GRIP, and GISP2 ice cores across MIS 2 and palaeoclimatic implications, Quaternary Science Reviews, 27, 18–28, https://doi.org/10.1016/j.quascirev.2007.01.016, 2008.

Rasmussen, S. O., Andersen, K. K., Svensson, A. M., Steffensen, J. P., Vinther, B. M., Clausen, H. B., Siggaard-Andersen, M. L., Johnsen, S. J., Larsen, L. B., Dahl-Jensen, D., Bigler, M., Röthlisberger, R., Fischer, H., Goto-Azuma, K., Hansson, M. E., and Ruth, U.: A new Greenland ice core chronology for the last glacial termination, Journal of Geophysical Research: Atmospheres, 111, 1–16, https://doi.org/10.1029/2005JD006079, 2006.

Rasmussen, S. O., Abbott, P. M., Blunier, T., Bourne, A. J., Brook, E., Buchardt, S. L., Buizert, C., Chappellaz, J., Clausen, H. B., Cook, E., Dahl-Jensen, D., Davies, S. M., Guillevic, M., Kipfstuhl, S., Laepple, T., Seierstad, I. K., Severinghaus, J. P., Steffensen, J. P., Stowasser, C., Svensson, A., Vallelonga, P., Vinther, B. M., Wilhelms, F., and Winstrup, M.: A first chronology for the north greenland eemian ice drilling (NEEM) ice core, Climate of the Past, 9, 2713–2730, https://doi.org/10.5194/cp-9-2713-2013, 2013.

Rasmussen, S. O., Bigler, M., Blockley, S. P., Blunier, T., Buchardt, S. L., Clausen, H. B., Cvijanovic, I., Dahl-Jensen, D., Johnsen, S. J., Fischer, H., et al.: A stratigraphic framework for abrupt climatic changes during the Last Glacial period based on three synchronized Greenland ice-core records: refining and extending the INTIMATE event stratigraphy, Quaternary Science Reviews, 106, 14–28, https://doi.org/10.1016/j.quascirev.2014.09.007, 2014.

Raynaud, D., Chappellaz, J., Ritz, C., and Martinerie, P.: Air content along the Greenland Ice Core Project core: A record of surface climatic parameters and elevation in central Greenland, Journal of Geophysical Research: Oceans, 102, 26 607–26 613, https://doi.org/10.1029/97JC01908, 1997.

Rignot, E. and Mouginot, J.: Ice flow in Greenland for the international polar year 2008–2009, Geophysical Research Letters, 39, 1–7, https://doi.org/10.1029/2012GL051634, 2012.

Riverman, K. L., Alley, R. B., Anandakrishnan, S., Christianson, K., Holschuh, N. D., Medley, B., Muto, A., and Peters, L. E.: Enhanced Firn Densification in High-Accumulation Shear Margins of the NE Greenland Ice Stream, Journal of Geophysical Research: Earth Surface, 124, 365–382, https://doi.org/10.1029/2017JF004604, 2019.

Robel, A. A., Degiuli, E., Schoof, C., and Tziperman, E.: Dynamics of ice stream temporal variability: Modes, scales, and hysteresis, Journal of Geophysical Research: Earth Surface, 118, 925–936, https://doi.org/10.1002/jgrf.20072, 2013.

Robin, G. d. Q. and Millar, D. H. M.: Flow Of Ice Sheets In The Vicinity Of Subglacial Peaks, Annals of Glaciology, 3, 290–294, https://doi.org/10.3189/s0260305500002949, 1982.

Robin, G. d. Q., Evans, S., and Bailey, J. T.: Interpretation of radio echo sounding in polar ice sheets, Philosophical Transactions of the Royal Society of London. Series A, Mathematical and Physical Sciences, 265, 437–505, https://doi.org/10.1098/rsta.1969.0063, 1969.

Salamatin, A. N., Lipenkov, V. Y., Barkov, N. I., Jouzel, J., Petit, J. R., and Raynaud, D.: Ice core age dating and paleothermometer calibration based on isotope and temperature profiles from deep boreholes at Vostok Station (East Antarctica), Journal of Geophysical Research: Atmospheres, 103, 8963–8977, https://doi.org/10.1029/97JD02253, 1998.

Seierstad, I. K., Abbott, P. M., Bigler, M., Blunier, T., Bourne, A. J., Brook, E., Buchardt, S. L., Buizert, C., Clausen, H. B., Cook, E., Dahl-Jensen, D., Davies, S. M., Guillevic, M., Johnsen, S. J., Pedersen, D. S., Popp, T. J., Rasmussen, S. O., Severinghaus, J. P., Svensson, A., and Vinther, B. M.: Consistently dated records from the Greenland GRIP, GISP2 and NGRIP ice cores for the past 104ka reveal regional millennial-scale δ18O gradients with possible Heinrich event imprint, Quaternary Science Reviews, 106, 29–46, https://doi.org/10.1016/j.quascirev.2014.10.032, 2014.

Shepherd, A., Ivins, E., Rignot, E., Smith, B., van den Broeke, M., Velicogna, I., Whitehouse, P., Briggs, K., Joughin, I., Krinner, G., Nowicki, S., Payne, T., Scambos, T., Schlegel, N., A, G., Agosta, C., Ahlstrøm, A., Babonis, G., Barletta, V. R., Bjørk, A. A., Blazquez, A., Bonin, J., Colgan, W., Csatho, B., Cullather, R., Engdahl, M. E., Felikson, D., Fettweis, X., Forsberg, R., Hogg, A. E., Gallee, H., Gardner, A., Gilbert, L., Gourmelen, N., Groh, A., Gunter, B., Hanna, E., Harig, C., Helm, V., Horvath, A., Horwath, M., Khan, S., Kjeldsen, K. K., Konrad, H., Langen, P. L., Lecavalier, B., Loomis, B., Luthcke, S., McMillan, M., Melini, D., Mernild, S., Mohajerani, Y., Moore, P., Mottram, R., Mouginot, J., Moyano, G., Muir, A., Nagler, T., Nield, G., Nilsson, J., Noël, B., Otosaka, I., Pattle, M. E., Peltier, W. R., Pie, N., Rietbroek, R., Rott, H., Sandberg Sørensen, L., Sasgen, I., Save, H., Scheuchl, B., Schrama, E., Schröder, L., Seo, K. W., Simonsen, S. B., Slater, T., Spada, G., Sutterley, T., Talpe, M., Tarasov, L., van de Berg, W. J., van der Wal, W., van Wessem, M., Vishwakarma, B. D., Wiese, D., Wilton, D., Wagner, T., Wouters, B., and Wuite, J.: Mass balance of the Greenland Ice Sheet from 1992 to 2018, Nature, 579, 233–239, https://doi.org/10.1038/s41586-019-1855-2, 2020.

Siegert, M.: On the origin, nature and uses of Antarctic ice-sheet radio-echo layering, Progress in Physical Geography, 23, 159–179, https://doi.org/10.1191/030913399671124903, 1999.

Simonsen, S. B. and Sørensen, L. S.: Implications of changing scattering properties on Greenland ice sheet volume change from Cryosat-2 altimetry, Remote Sensing of Environment, 190, 207–216, https://doi.org/10.1016/j.rse.2016.12.012, 2017.

Smith-Johnsen, S., De Fleurian, B., Schlegel, N., Seroussi, H., and Nisancioglu, K.: Exceptionally high heat flux needed to sustain the Northeast Greenland Ice Stream, Cryosphere, 14, 841–854, https://doi.org/10.5194/tc-14-841-2020, 2020a.

Smith-Johnsen, S., Schlegel, N. J., de Fleurian, B., and Nisancioglu, K. H.: Sensitivity of the Northeast Greenland Ice Stream to Geothermal Heat, Journal of Geophysical Research: Earth Surface, 125, 1–14, https://doi.org/10.1029/2019JF005252, 2020b.

Svensson, A., Andersen, K. K., Bigler, M., Clausen, H. B., Dahl-Jensen, D., Davies, S. M., Johnsen, S. J., Muscheler, R., Rasmussen, S. O., Röthlisberger, R., et al.: The Greenland ice core chronology 2005, 15–42 ka. Part 2: comparison to other records, Quaternary Science Reviews, 25, 3258–3267, https://doi.org/10.1029/2005JD006079, 2006.

Svensson, A., Andersen, K. K., Bigler, M., Clausen, H. B., Dahl-Jensen, D., Davies, S. M., Johnsen, S. J., Muscheler, R., Parrenin, F., Rasmussen, S. O., Röthlisberger, R., Seierstad, I., Steffensen, J. P., and Vinther, B. M.: A 60 000 year Greenland stratigraphic ice core chronology, Climate of the Past, 4, 47–57, https://doi.org/10.5194/cp-4-47-2008, 2008.

Tulaczyk, S., Kamb, W. B., and Engelhardt, H. F.: Basal mechanics of Ice Stream B, West Antarctica: 1. Till mechanics, Journal of Geophysical Research: Solid Earth, 105, 463–481, https://doi.org/10.1029/1999jb900329, 2000.

Vallelonga, P., Christianson, K., Alley, R., Anandakrishnan, S., Christian, J., Dahl-Jensen, D., Gkinis, V., Holme, C., Jacobel, R., Karlsson, N., et al.: Initial results from geophysical surveys and shallow coring of the Northeast Greenland Ice Stream (NEGIS), The Cryosphere, 8, 1275–1287, https://doi.org/10.5194/tc-8-1275-2014, 2014.

Vinther, B., Buchardt, S., Clausen, H., Dahl-Jensen, D., Johnsen, S., Fisher, D., Koerner, R., Raynaud, D., Lipenkov, V., Andersen, K. K., et al.: Holocene thinning of the Greenland ice sheet, Nature, 461, 385–388, https://doi.org/10.1038/nature08355, 2009.

Vinther, B. M., Clausen, H. B., Johnsen, S. J., Rasmussen, S. O., Andersen, K. K., Buchardt, S. L., Dahl-Jensen, D., Seierstad, I. K., Siggaard-Andersen, M.-L., Steffensen, J. P., et al.: A synchronized dating of three Greenland ice cores throughout the Holocene, Journal of Geophysical Research: Atmospheres, 111, https://doi.org/10.1029/2005JD006921, 2006.

Waddington, E. D., Neumann, T. A., Koutnik, M. R., Marshall, H. P., and Morse, D. L.: Inference of accumulation-rate patterns from deep layers in glaciers and ice sheets, Journal of Glaciology, 53, 694–712, https://doi.org/10.3189/002214307784409351, 2007.

Walker, M., Johnes, S., Rasmussen, S. O., Popp, T., Steffensen, J.-P., Gibbard, P., Hoek, W., Lowe, J., Andrews, J., Björck, S., Cwynar, L. C., Hughen, K., Kershaw, P., Kromer, B., Litt, T., Lowe, D. J., Nakagawa, T., Newnham, R., and Schwander, J.: Formal definition and dating of the GSSP (Global Stratotype Section and Point) for the base of the Holocene using the Greenland NGRIP ice core, and selected auxiliary records, Journal of Quaternary Science, 24, 3–17, https://doi.org/10.1002/jqs, 2009.

Weertman, J.: Sliding–no sliding zone effect and age determination of ice cores, Quaternary Research, 6, 203–207, https://doi.org/10.1016/0033-5894(76)90050-8, 1976.

Whillans, I. M.: Radio-echo layers and the recent stability of the West Antarctic ice sheet, Nature, 264, 152–155, https://doi.org/10.1038/264152a0, 1976.

Whillans, I. M. and Johnsen, S. J.: Longitudinal variations in glacial flow: theory and test using data from the Byrd Station strain network, Antarctica., Journal of Glaciology, 29, 78–97, https://doi.org/10.1017/S0022143000005165, 1983.

Wolovick, M. J., Creyts, T. T., Buck, W. R., and Bell, R. E.: Traveling slippery patches produce thickness-scale folds in ice sheets, Geophysical Research Letters, 41, 8895–8901, https://doi.org/10.1002/2014GL062248, 2014.

Yiou, F., Raisbeck, G. M., Baumgartner, S., Beer, J., Hammer, C., Johnsen, S., Jouzel, J., Kubik, P. W., Lestringuez, J., Stiévenard, M., Suter, M., and Yiou, P.: Beryllium 10 in the Greenland Ice Core Project ice core at Summit, Greenland, Journal of Geophysical Research: Oceans, 102, 26 783–26 794, https://doi.org/10.1029/97JC01265, 1997.

Zeising, O. and Humbert, A.: Indication of high basal melting at EastGRIP drill site on the Northeast Greenland Ice Stream, The Cryosphere Discussions, pp. 1–15, https://doi.org/10.5194/tc-2021-37, 2021.